

Majorana representation for topological edge states of massless Dirac fermion with non-quantized Berry phase

F. R. Pratama^{1,2*} and Takeshi Nakanishi^{1†}

¹*Mathematics for Advanced Materials-OIL, AIST, 2-1-1 Katahira, Aoba, 980-8577 Sendai, Japan*

²*Advanced Institute for Materials Research, Tohoku University, 2-1-1 Katahira, Aoba, 980-8577 Sendai, Japan*

(Dated: June 27, 2024)

We study the bulk-boundary correspondences for zigzag ribbons (ZRs) of massless Dirac fermion in two-dimensional α - T_3 lattice. By tuning the hopping parameter $\alpha \in [0, 1]$, the α - T_3 lattice interpolates between pseudospin $S = 1/2$ (graphene) and $S = 1$ (T_3 or dice lattice), for $\alpha = 0$ and 1 , respectively, which is followed by continuous change of the Berry phase from π to 0 . The range of existence for edge states in the momentum space is determined by solving tight-binding equations at the boundaries of the ZRs. We find that the transitions of in-gap bands from bulk to edge states in the momentum space do not only occur at the positions of the Dirac cones but also at additional points depending on $\alpha \notin \{0, 1\}$. The α - T_3 ZRs are mapped into stub Su-Schrieffer-Heeger chains by performing unitary transforms of the bulk Hamiltonian. The non-trivial topology of the bulk bands is revealed by the Majorana representation of the eigenstates, where the \mathbb{Z}_2 topological invariant is manifested by the winding numbers on the complex plane and the Bloch sphere.

PACS numbers: 72.20.Pa, 72.10.-d, 73.50.Lw

I. INTRODUCTION

Bulk-boundary correspondence (BBC) is the relation between the number of robust edge states and the bulk topological invariant. This concept leads to the paradigm [1–3] to classify phases of condensed-matters based on the topology of bulk bands. The pioneering work of Thouless *et. al.* [4] identified the Chern number \mathcal{C} of the occupied Landau levels as the \mathbb{Z} invariant for the quantized Hall conductivity [5] in a non-interacting, two-dimensional (2D) electron gas. In systems that preserve time-reversal symmetry, \mathbb{Z}_2 invariants [6] differentiate between the ordinary and quantum spin Hall insulators.

The Berry phase [7] in 1D Brillouin zone (BZ), also known as the Zak phase [8], provides the \mathbb{Z}_2 invariant for the Dirac matters with both time-reversal and inversion symmetries [9]. The quantized value of Zak phase to π or 0 is utilized to predict the presence or absence of edge states in the Su-Schrieffer-Heeger (SSH) chain of polyacetylene [10] and in various types of graphene ribbons [11–14], insofar the number of unit cells is commensurate with the bulk lattice [15]. The spinless model for these systems is described by the generic Hamiltonian $\mathcal{H} = \mathbf{d} \cdot \boldsymbol{\sigma}$, where $\boldsymbol{\sigma} = (\sigma_x, \sigma_y, \sigma_z)$ is the vector of Pauli matrices. The bivalued Zak phase corresponds to the two possibilities whether the path of $\mathbf{d} = (\text{Re}[\mathbf{d}], -\text{Im}[\mathbf{d}], 0)$ encloses the origin of the complex plane or not [16, 17]. \mathcal{H} is also adapted to explain the edge states in phosphorene ribbons [18–21]. Experimentally, the topology of SSH chain is studied by using arrays of cold atoms [22–26], photonic waveguides [27–30], and electrical circuits [31]. Apart from the observations [32–34] by scanning-tunneling microscopy, the properties of edge

states in graphene ribbons have been investigated using artificial honeycomb lattices [35], which encompass the photonic [36–41], phononic [42, 43], plasmonic [44, 45], and polaritonic [46, 47] analogs of graphene.

The α - T_3 lattice [48] [Fig. 5(a)] interpolates between pseudospin $S = 1/2$ (graphene [49]) and $S = 1$ (T_3 or dice lattice [50, 51]) by continuously varying the hopping parameter α from 0 to 1 , respectively, while the energy dispersion [Fig. 5(b)] remains the same. On the other hand, the Berry phase smoothly changes from π to 0 , which can be seen in the gradual transition of diamagnetic to paramagnetic orbital susceptibilities [48], among others. Motivated by the unconventional physics phenomena that arise from the variable geometric phase and the existence of flat band—e.g. enhanced Klein tunneling and supercollimation [52–57]—there have been extensive studies on the properties of the T_3 and α - T_3 lattices, including the optical [58–65], magnetic [48, 66–68], pseudomagnetic [69–71], magneto-optical [72–75], and transport [76–84] properties. The T_3 lattice is predicted to occur in several perovskite-based heterostructures [85, 86] and strained blue-phosphorene oxide [87]. Moreover, the Hamiltonian of the α - T_3 lattice can be employed to reproduce the absorption spectra [88] of 2D $\text{Hg}_{1-x}\text{Cd}_x\text{Te}$ at the critical doping $x \approx 0.17$ [89].

In the context of topology, the T_3 lattice shows quantum anomalous Hall effect with $|\mathcal{C}| = 2$ [90, 91] by including the Haldane term [92] in the Hamiltonian. Similarly, the α - T_3 ribbon with spin-orbit interactions shows the quantum spin Hall effect [93]. However, the BBC for the α - T_3 lattice without opening non-trivial gaps is yet to be formulated, even though it is natural to investigate whether the topological edge states remain without the quantized Berry phase. Furthermore, it is shown in a recent work [94] that the T_3 zigzag ribbon (ZR) hosts edge states. Our study shows that the edge states are topologically non-trivial despite the zero Berry phase.

* pratama.fr@aist.go.jp

† t.nakanishi@aist.go.jp

Our paper is organized as follows. In Sec. II, we discuss the BBC for the stub SSH chain [95–97], which is constructed by connecting an additional site to one of the sites in the SSH dimer as depicted in Fig. 1. The results of this section are useful for understanding and will be applied to uncover the BBC of the α - T_3 ZRs. In the Majorana representation of the eigenstates [98–100], we analytically prove that the presence or absence of edge states are topologically characterized by winding numbers on the complex plane and the Bloch sphere. Sec. III is devoted to a brief review of the relevant bulk properties of the α - T_3 lattice. In Sec. IV, first we describe the configurations of α - T_3 ZR. For two types of ZRs, tight-binding equations (TBEs) at the boundaries are solved to determine the range of existence for edge states in momentum space. In Sec. V, we map the α - T_3 ZRs into stub SSH chains by unitary transforms of the Hamiltonian. Here, momentum in the direction parallel to the α - T_3 ZRs is transformed into hopping parameters of the corresponding stub SSH chains, and thus the dimension is reduced from 2D to 1D. We discuss the topological phase diagram for each ZR. Conclusion is given in Sec. VI.

This paper serves as a technical companion to Ref. [101] by providing detailed derivations of the results.

II. STUB SSH CHAIN

A. Bulk Hamiltonian

Fig. 1 illustrates the stub SSH chain. In each unit cell (dashed rectangle), the intracell hopping parameter between the B and A (C) sites is $V_A \geq 0$ (V_C). The intercell hopping parameter is V'_A . For a chain consisting J unit cells, the Hamiltonian \hat{H} is given by

$$\hat{H} = - \sum_{j=1}^J \left[V_A \left(\hat{a}_j^\dagger \hat{b}_j + \hat{b}_j^\dagger \hat{a}_j \right) + V'_A \left(\hat{a}_j^\dagger \hat{b}_{j+1} + \hat{b}_{j+1}^\dagger \hat{a}_j \right) + V_C \left(\hat{b}_j^\dagger \hat{c}_j + \hat{c}_j^\dagger \hat{b}_j \right) \right], \quad (1)$$

where \hat{a}_j^\dagger , \hat{b}_j^\dagger , and \hat{c}_j^\dagger (\hat{a}_j , \hat{b}_j , and \hat{c}_j) are the creation (annihilation) operators for the A , B , and C sites, respectively, in the j -th unit cell. By performing the Fourier transforms for the creation and annihilation operators, the bulk Hamiltonian in the momentum space is given by $\hat{H}(k) = \sum_k \hat{\Psi}_k^\dagger H(k) \hat{\Psi}_k$, where $\hat{\Psi}_k = (a_k \ b_k \ c_k)^T$ is the field operator, and

$$H(k) = - \begin{bmatrix} 0 & F^*(k) & 0 \\ F(k) & 0 & V_C \\ 0 & V_C & 0 \end{bmatrix}. \quad (2)$$

Here, we define

$$F(k) = |F(k)| e^{-i\Phi(k)} \equiv V_A + V'_A e^{-ika_0}. \quad (3)$$

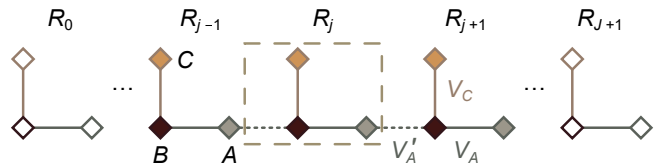


FIG. 1. The stub SSH chain. The position of j -th unit cell (dashed rectangle) is denoted by R_j , for $j = 1, 2, \dots, J$, where J is the number of unit cells. The intracell (intercell) hopping parameter between the A and B sites is V_A (V'_A), and that between the C and B sites is V_C . The unfilled symbols at R_0 and R_{j+1} indicate missing sites.

$a_0 \equiv R_{j+1} - R_j$ is the lattice constant [102]. $\Phi(k) \in (-\pi, \pi]$ is given by [103]:

$$\Phi(k) = \text{Arg} \left[\frac{V_A}{V'_A} + \cos(ka_0) + i \sin(ka_0) \right]. \quad (4)$$

Without loss of generality, we only consider $V'_A > 0$, and the 1D BZ is defined for $k \in [-\pi/a_0, \pi/a_0]$ [104]. It is noted that $F(-k) = F^*(k)$ and $\Phi(-k) = -\Phi(k)$.

The energy eigenvalues of Eq. (2) are given by

$$E_s(k) = s \sqrt{V_A^2 + V'_A{}^2 + V_C^2 + 2V_A V'_A \cos(ka_0)}, \quad (5a)$$

$$E_0 = 0, \quad (5b)$$

where E_s indicates the valence (conduction) band for $s = -1$ ($+1$). E_0 is the flat band at zero energy whose origin is understood from the Lieb theorem [105]: due to the absence of interactions between the A and C sites, each unit cell can be partitioned into two sublattices: one consists of the A and C sites, the other consists of the B site. The numerical imbalance between the sublattices gives rise to E_0 . For $V_C \neq 0$, the bulk bands do not touch at $|k| = \pi/a_0$, unlike in the SSH chain where the gap closing indicates a topological phase transition when $V_A/V'_A = 1$. Nevertheless, regardless the value of V_C ,

$$\Phi \left(\frac{\pi}{a_0} \right) = \begin{cases} \pi & \text{for } V_A/V'_A < 1, \\ 0 & \text{for } V_A/V'_A > 1, \end{cases} \quad (6)$$

and indeterminate for $V_A/V'_A = 1$. Eq. (6) will be used to calculate the topological index.

The eigenvectors for the band $c \in \{s, 0\}$ are

$$|\Psi_s(k)\rangle = \frac{1}{\sqrt{2}} \begin{bmatrix} \cos \Theta(k) e^{i\Phi(k)} \\ s \\ \sin \Theta(k) \end{bmatrix} \quad (7a)$$

for the dispersive bands, and

$$|\Psi_0(k)\rangle = \begin{bmatrix} \sin \Theta(k) e^{i\Phi(k)} \\ 0 \\ -\cos \Theta(k) \end{bmatrix} \quad (7b)$$

for the flat band, where $\Theta(k) \equiv \tan^{-1}(V_C/|F(k)|)$.

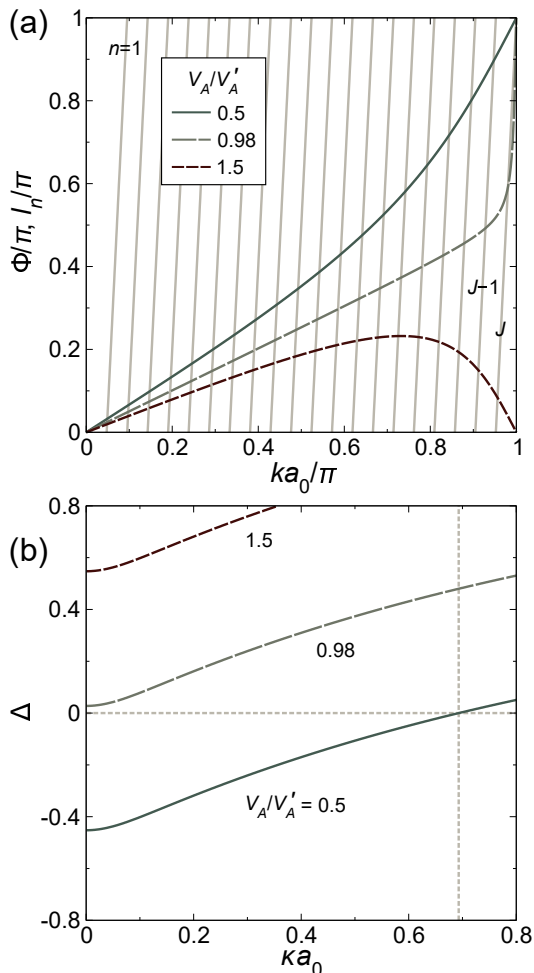


FIG. 2. (a) Plot of $\Phi(k)$ for $V_A/V'_A = 0.5, 0.98, \text{ and } 1.5$. The straight lines are $l_n(k) = (J+1)ka_0 - n\pi$ for $n = 1, 2, \dots, J$, where $J = 20$. (b) Plot of $\Delta(\kappa)$ for the same values of V_A/V'_A . The vertical and horizontal dashed lines are located at $\kappa a_0 \approx 0.693$ and $\Delta = 0$, respectively.

B. Open boundary conditions

We derive the quantization condition of k to enumerate the number of bulk states by imposing the boundary conditions on the wavefunction $\Psi_s = (\Psi_s^A \ \Psi_s^B \ \Psi_s^C)^T$.

1. Missing bulk states

As illustrated by Fig. 1, the missing B site at R_{J+1} and A site at R_0 necessitate

$$\Psi_s^B(R_{J+1}) = 0, \quad (8)$$

$$\Psi_s^A(R_0) = 0. \quad (9)$$

$\Psi_s(R_j)$ is constructed by a linear combination of the Bloch states with opposite momenta as follows [11, 106]:

$$\Psi_s(R_j) \equiv \mathcal{A}_+ e^{ikR_j} |\Psi_s(k)\rangle + \mathcal{A}_- e^{-ikR_j} |\Psi_s(-k)\rangle. \quad (10)$$

By letting $R_j = (j-J-1)a_0$, Eq. (8) implies $\mathcal{A}_- = -\mathcal{A}_+$. Thus, Eq. (9) yields

$$e^{-i(J+1)ka_0} F^*(k) = e^{i(J+1)ka_0} F(k) \quad (11)$$

or $\sin[(J+1)ka_0 - \Phi(k)] = 0$. Equivalently, the quantization condition of k for a finite J is given by

$$(J+1)ka_0 - \Phi(k) = n\pi, \text{ for } n = 1, 2, \dots, J. \quad (12)$$

In Fig. 2(a), we plot $\Phi(k)$ as a function of $k \in [0, \pi/a_0]$ for $V_A/V'_A = 0.5, 0.98, \text{ and } 1.5$. The straight lines correspond to $l_n(k) \equiv (J+1)ka_0 - n\pi$, for $J = 20$. The number of bulk states is equal to the number of solutions of Eq. (12), which are given by the intersections of $\Phi(k)$ and $l_n(k)$ along $k \in (0, \pi/a_0)$. Here, $\Psi_s(R_j)$ vanishes identically at $k \in \{0, \pi/a_0\}$. There are J solutions for $V_A/V'_A = 0.98$ and 1.5 . On the other hand, one solution is missing for $V_A/V'_A = 0.5$. The existence of $J-1$ solutions requires $\Phi(\pi/a_0) = \pi$ and $\partial_k \Phi(k)|_{\pi/a_0} < \partial_k l_J(k)|_{\pi/a_0}$, or

$$V_A/V'_A < 1 - 1/(J+1). \quad (13)$$

We shall show that edge states emerge from the missing bulk states. The ratio $(V_A/V'_A)_J \equiv 1 - 1/(J+1)$ is interpreted as the critical value of V_A/V'_A at which a bulk state for each $E < 0$ and $E > 0$ become edge states. In the limit $J \rightarrow \infty$, $(V_A/V'_A)_\infty \sim 1$.

2. Edge states

By substituting $k = \pi/a_0 + i\kappa$ into Eqs. (3) and (11),

$$e^{(J+1)\kappa a_0} \tilde{F}(-\kappa) = e^{-(J+1)\kappa a_0} \tilde{F}(\kappa), \quad (14)$$

where we define

$$\tilde{F}(\kappa) \equiv V_A - V'_A e^{\kappa a_0}. \quad (15)$$

Here, $1/\kappa > 0$ is the localization length of edge states. By rearranging Eq. (14), κ satisfies

$$\Delta(\kappa) \equiv \frac{V_A}{V'_A} - \frac{\sinh[J\kappa a_0]}{\sinh[(J+1)\kappa a_0]} = 0. \quad (16)$$

In Fig. 2(b), we plot $\Delta(\kappa)$ for $V_A/V'_A = 0.5, 0.98$ and 1.5 . Eq. (16) is satisfied for $V_A/V'_A = 0.5$, where $\Delta(\kappa) = 0$ at $\kappa \approx 0.693/a_0$ (vertical dashed line). Thus, the edge states exist for

$$\frac{V_A}{V'_A} = \frac{\sinh[J\kappa a_0]}{\sinh[(J+1)\kappa a_0]} < 1. \quad (17)$$

By inserting $k = \pi/a_0 + i\kappa$ into Eq. (5a), the energies of edge states are given by

$$\tilde{E}_s(\kappa) = s\sqrt{V_A^2 + V'_A{}^2 + V_C^2 - 2V_A V'_A \cosh(\kappa a_0)}. \quad (18)$$

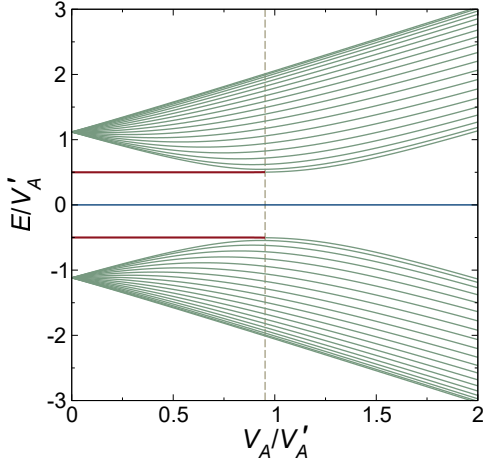


FIG. 3. Energy spectra of the stub SSH chain as a function of V_A/V'_A for $V_C = 0.5V'_A$ and $J = 20$. The bold red lines indicate the edge states. The blue line at $E = 0$ is the flat band. The transition from bulk to edge states occurs at $(V_A/V'_A)_{20} \approx 0.9524$ (vertical dashed line), where $|E| \sim |V_C|$.

By combining Eqs. (17) and (18), we get

$$\tilde{E}_s(\kappa) \equiv s \sqrt{V_A'^2 \frac{\sinh^2(\kappa a_0)}{\sinh^2[(J+1)\kappa a_0]} + V_C^2}. \quad (19)$$

$$\mathcal{Z}_s = - \int_0^{\pi/a_0} dk \cos^2 \Theta(k) \frac{\partial \Phi(k)}{\partial k} = -\frac{\pi}{2} \left[1 - \frac{V_A^2 - V_A'^2 + V_C^2}{\sqrt{(V_A - V_A')^2 + V_C^2} \sqrt{(V_A + V_A')^2 + V_C^2}} \right], \quad (20a)$$

$$\mathcal{Z}_0 = -2 \int_0^{\pi/a_0} dk \sin^2 \Theta(k) \frac{\partial \Phi(k)}{\partial k} = -\pi \left[1 - \text{sgn}(V_A^2 - V_A'^2) \right] - 2\mathcal{Z}_s. \quad (20b)$$

The case $V_C = 0$ corresponds to the SSH chain with an additional flat band originating from the uncoupled C sites, where $\mathcal{Z}_s = -\pi$ and 0 for $V_A/V'_A < 1$ and $V_A/V'_A > 1$, respectively, and hence $|\mathcal{Z}_s| = \Phi(\pi/a_0)$. This relation does not hold for $V_C \neq 0$. On the other hand, it was shown [97] that the edge states in the stub SSH chain are robust against disorders that perturb V_A and V'_A , which suggests the topologically non-trivial character of the bulk bands. By using the Majorana representation of the eigenstates, Bartlett *et al.* [96] found that the existence of the edge states can be predicted from the azimuthal winding number W_c on the Bloch sphere. We complement the finding with an analytical proof that $|W_c| = \Phi(\pi/a_0)$.

The Majorana representation is a method to visualize the eigenstate $|\Psi\rangle$ of an $N \times N$ Hamiltonian on the Bloch sphere by a set pseudospinors for $S = 1/2$. Here, $|\Psi\rangle$ is treated as a pseudospinor for $S = (N-1)/2$. According

We can see that for $J\kappa a_0 \gg 1$, $\tilde{E}_s(\kappa)$ becomes independent of J and converges to $\tilde{E}_s \sim s|V_C|$.

Fig. 3 shows the numerical calculation of energy spectra as a function of V_A/V'_A for $V_C = 0.5V'_A$ and $J = 20$. Since each unit cell consists of three sites, there exist $3J$ bands in total: J pairs of dispersive bands and a flat band with J -fold degeneracy at $E = 0$ (blue line). The edge states are depicted by the bold red lines. The transition from bulk to edge states is marked by the vertical dashed line at $(V_A/V'_A)_{20} \approx 0.9524$, where the in-gap bands become constant at $|E| \sim |V_C|$. Therefore, the emergence of edge states is indicated by the flattening of the in-gap bands when $V_A/V'_A < 1$. Our theoretical result is consistent with a recent experiment [97] that realized stub SSH chain using a photonic lattice.

C. Topological invariant

We have demonstrated that the emergence of edge states in the stub SSH chain is irrespective of V_C and controlled only by V_A/V'_A , similar to the SSH chain. Nevertheless, the presence of the coupled C sites breaks the inversion symmetry [96], and as a consequence, the Zak phase $\mathcal{Z}_c \equiv i \int_{\text{BZ}} dk \langle \Psi_c(k) | \partial_k | \Psi_c(k) \rangle$ is no longer quantized to π and $0 \pmod{2\pi}$. By using $|\Psi_c\rangle$ in Eqs. (7a) and (7b), \mathcal{Z}_c 's are analytically calculated as follows:

to the Schwinger theory [107] of angular momentum, $|\Psi\rangle$ can be constructed by the bosonic creation operators $\hat{a}_{\uparrow, \downarrow}^\dagger$ acting on the vacuum state $|\emptyset\rangle$, as follows:

$$|\Psi\rangle = \sum_{\mu=-S}^S \mathcal{C}_\mu \frac{(\hat{a}_{\uparrow}^\dagger)^{S+\mu}}{\sqrt{(S+\mu)!}} \frac{(\hat{a}_{\downarrow}^\dagger)^{S-\mu}}{\sqrt{(S-\mu)!}} |\emptyset\rangle, \quad (21)$$

where \mathcal{C}_μ 's are the basis vector. Earlier, Majorana [98] discovered that $|\Psi\rangle$ is given by a product of the Pauli spinors $|\zeta_\mu\rangle = [\cos(\eta_\mu/2) \sin(\eta_\mu/2) e^{i\xi_\mu}]^T$ as follows:

$$\begin{aligned} |\Psi\rangle &= \frac{1}{\mathcal{K}} \prod_{\mu=1}^{2S} \left[\cos\left(\frac{\eta_\mu}{2}\right) \hat{a}_{\uparrow}^\dagger + \sin\left(\frac{\eta_\mu}{2}\right) e^{i\xi_\mu} \hat{a}_{\downarrow}^\dagger \right] |\emptyset\rangle \\ &= \frac{1}{\mathcal{K}} \prod_{\mu=1}^{2S} |\zeta_\mu\rangle, \end{aligned} \quad (22)$$

where \mathcal{K} is the normalization constant. η and ξ are the polar and azimuthal angles. The trajectory of each Majorana 'star' $\zeta_\mu \equiv \langle \zeta_\mu | \sigma | \zeta_\mu \rangle$ thus represents the evolution of $|\Psi\rangle$. Alternatively, Eq. (22) is expressed as

$$|\Psi\rangle = \frac{\mathcal{C}_S}{\sqrt{(2S)!}} \prod_{\mu=1}^{2S} [\hat{a}_\uparrow^\dagger + \lambda_\mu \hat{a}_\downarrow^\dagger] |\emptyset\rangle, \quad (23)$$

where $\lambda_\mu = \tan(\eta_\mu/2)e^{i\xi_\mu}$. Suppose that λ_μ 's are the roots of $\prod_{\mu=1}^{2S} (\lambda - \lambda_\mu) = 0$. By comparing the coefficients of Eqs. (21) and (23), λ_μ are given by the Majorana polynomial as follows:

$$\sum_{\mu=0}^{2S} (-1)^\mu \frac{\mathcal{C}_S - \mu}{\sqrt{(2S - \mu)! \mu!}} \lambda^{2S - \mu} = 0. \quad (24)$$

Particularly for the stub SSH chain, we insert $S = 1$, where $|\Psi\rangle = (\mathcal{C}_1 \ \mathcal{C}_0 \ \mathcal{C}_{-1})^T$ is given by Eqs. (7a) or (7b). For the dispersive band, Eq. (24) is reduced to

$$\cos \Theta(k) e^{i\Phi(k)} \lambda^2 - \sqrt{2} s \lambda + \sin \Theta(k) = 0. \quad (25a)$$

As for the flat band, we get

$$\sin \Theta(k) e^{i\Phi(k)} \lambda^2 - \cos \Theta(k) = 0. \quad (25b)$$

The winding number Ω_c around the origin of complex plane is calculated by the Cauchy integral formula. Let $\lambda_s^\mp(k)$ and $\lambda_0^\mp(k)$ be the roots of Eqs. (25a) and (25b), respectively. From the coefficients of the quadratic equations, it is noted that

$$\Lambda_s(k) \equiv \prod_{\nu=\mp} \lambda_s^\nu(k) = \tan \Theta(k) e^{-i\Phi(k)}, \quad (26a)$$

$$\Lambda_0(k) \equiv \prod_{\nu=\mp} \lambda_0^\nu(k) = -\cot \Theta(k) e^{-i\Phi(k)}. \quad (26b)$$

By regarding $\Lambda_c(k)$ as a curve parameterized by k ,

$$\Omega_c \equiv \frac{1}{2\pi i} \int_{-\pi/a_0}^{\pi/a_0} \frac{dk}{\Lambda_c(k)} \frac{\partial \Lambda_c(k)}{\partial k}. \quad (27)$$

Here, $d \ln \Lambda_s(k) = d \ln |\tan \Theta(k)| - i d \Phi(k)$ and $d \ln \Lambda_0(k) = d \ln |\cot \Theta(k)| - i d \Phi(k)$. It is noted that $\Lambda_c(k)$ is a closed curve because $\Theta(-\pi/a_0) = \Theta(\pi/a_0)$, thus the total changes of $\ln |\tan \Theta(k)|$ and $\ln |\cot \Theta(k)|$ are zero. Therefore, Ω_c is identical for each c as follows:

$$\Omega_c = -\frac{1}{2\pi} \int_{-\pi/a_0}^{\pi/a_0} dk \frac{\partial \Phi(k)}{\partial k} = -\frac{1}{\pi} \Phi \left(\frac{\pi}{a_0} \right). \quad (28)$$

The azimuthal winding number W_c counts for the total number of times $\zeta_c^\nu(k)$'s travel around the z axis of the Bloch sphere. W_c is defined by [96]:

$$W_c \equiv \frac{1}{2\pi} \int_{-\pi/a_0}^{\pi/a_0} dk \frac{\partial}{\partial k} \sum_{\nu=\mp} \xi_c^\nu(k). \quad (29)$$

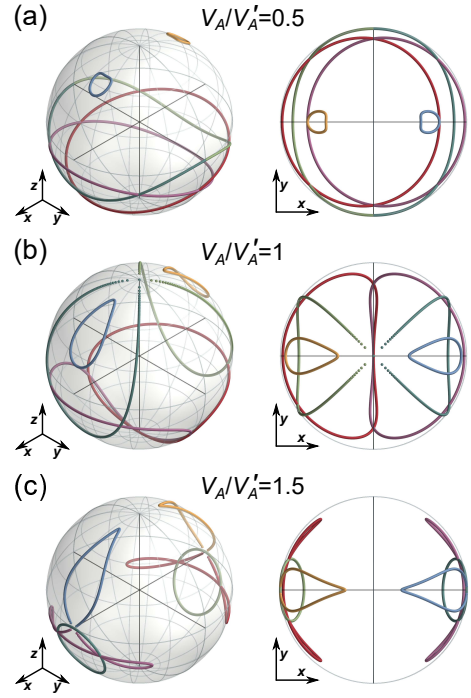


FIG. 4. Trajectories of the Majorana stars on the Bloch sphere (left panels) and the xy plane (right panels) for $V_C = 0.5V'_A$, and (a) $V_A/V'_A = 0.5$, (b) 1, (c) 1.5. The red and yellow (blue and purple) curves correspond to the valence (conduction) band, $c = -1$ ($c = +1$). The light-green and dark-green curves correspond to the flat band, $c = 0$.

Since $\lambda_c^\nu(k) = \tan[\eta_c^\nu(k)/2]e^{i\xi_c^\nu(k)}$ by definition,

$$-\sum_{\nu=\mp} \xi_c^\nu(k) = \Phi(k). \quad (30)$$

By substituting Eq. (30) into Eq. (29), it is inferred that $W_c = \Omega_c$, and accordingly:

$$|W_c| = \begin{cases} 1 & \text{for } V_A/V'_A < 1, \\ 0 & \text{for } V_A/V'_A > 1. \end{cases} \quad (31)$$

Therefore, the trajectories of $\zeta_c^\nu(k)$'s enclose the z axis once only if $\Phi(\pi/a_0) = \pi$, as k is traversing the BZ.

Fig. 4 shows the trajectories of ζ_c^ν 's on the Bloch sphere (left panels) and their projections on the xy plane (right panels) for $V_C = 0.5V'_A$, and (a) $V_A/V'_A = 0.5$, (b) 1, (c) 1.5. ζ_c^ν 's associated with $c = -1, 0$, and 1 are depicted by the red/yellow, light-green/dark-green, and blue/purple curves, respectively. In Fig. 4(a), the red, purple, and connected green loops wind around the z axis, so $|W_c| = 1$. In Fig. 4(b), $|W_c|$ is ill-defined because the same loops intersect the poles. This is an example of topological phase transition without gap closing, which can occur provided that the topological invariant at the transition point becomes ill-defined [108]. In Fig. 4(c), none of the curves enclose the z axis and thus $|W_c| = 0$.

It is noted that Eqs. (31) does not hold for all of the bases of $|\Psi_c\rangle$. Hereafter, the basis in Eqs. (7a) or (7b) is referred to as (abc) for simplicity. There are six permutations of basis in total: (abc) , (bca) , (cab) , (cba) , (acb) , and (bac) . In general, the \mathbb{Z}_2 invariant is given by the parity P of the total winding numbers defined by [96]:

$$P \equiv (-1)^{\sum_c |W_c|}, \quad (32)$$

where $P = -1$ and $+1$ indicate the non-trivial and trivial phases, respectively. We prove this statement by calculating the Majorana polynomials for all the bases, which are classified into three cases as follows:

1. For (abc) and (cba) , $\Lambda_c \propto e^{-i\Phi}$ and $e^{i\Phi}$, respectively.
 2. For (bca) and (acb) , $\Lambda_s \propto e^{i\Phi}$ and $e^{-i\Phi}$, respectively, while a single solution of the Majorana polynomial for the flat band is $\lambda_0 \propto e^{i\Phi}$ and $e^{-i\Phi}$, respectively.
 3. For (cab) and (bac) , Λ_s does not depend on Φ , and $\lambda_0 \propto e^{i\Phi}$ and $e^{-i\Phi}$, respectively, for the single solution.
- By calculating W_c , $\sum_c |W_c| = 0$ for all cases when $V_A/V'_A > 1$. In contrast, $\sum_c |W_c|$ is either 3 (cases 1 and 2) or 1 (case 3) when $V_A/V'_A < 1$. Therefore,

$$P = \begin{cases} -1 & \text{for } V_A/V'_A < 1, \\ +1 & \text{for } V_A/V'_A > 1. \end{cases} \quad (33)$$

III. α - T_3 LATTICE

Consider a honeycomb lattice composed of A and B sites. The α - T_3 lattice is constructed by connecting the additional C sites at the center of each hexagon to the nearest B sites, as illustrated by Fig. 5(a). The nearest-neighbour interactions between the B and A (C) sites are denoted by the hopping parameter $t_A > 0$ (t_C), where $t_C/t_A = \alpha \in [0, 1]$. The dashed hexagons represent three choices to define the unit cell. The vectors $\mathbf{b}_1 = a(-1/2, -1/2\sqrt{3})$, $\mathbf{b}_2 = a(1/2, -1/2\sqrt{3})$ and $\mathbf{b}_3 = a(0, 1/\sqrt{3})$ connect the B site to the nearest A and C sites, where a is the length of primitive vectors $\mathbf{a}_1 = a(1, 0)$ and $\mathbf{a}_2 = a(1/2, \sqrt{3}/2)$.

The bulk Hamiltonian $h(\mathbf{k})$ in the momentum space $\mathbf{k} = (k_x, k_y)$ is given by

$$h(\mathbf{k}) = - \begin{bmatrix} 0 & t_A f(\mathbf{k}) & 0 \\ t_A f^*(\mathbf{k}) & 0 & t_C f(\mathbf{k}) \\ 0 & t_C f^*(\mathbf{k}) & 0 \end{bmatrix}, \quad (34)$$

where we define

$$f(\mathbf{k}) \equiv \sum_{n=1}^3 e^{-i\mathbf{k}\cdot\mathbf{b}_n} = |f(\mathbf{k})| e^{-i\varphi(\mathbf{k})}. \quad (35)$$

By defining $t \equiv \sqrt{t_A^2 + t_C^2}$ and $\vartheta \equiv \tan^{-1} \alpha$,

$$h(\mathbf{k}) = -t \begin{bmatrix} 0 & \cos \vartheta f(\mathbf{k}) & 0 \\ \cos \vartheta f^*(\mathbf{k}) & 0 & \sin \vartheta f(\mathbf{k}) \\ 0 & \sin \vartheta f^*(\mathbf{k}) & 0 \end{bmatrix}. \quad (36)$$

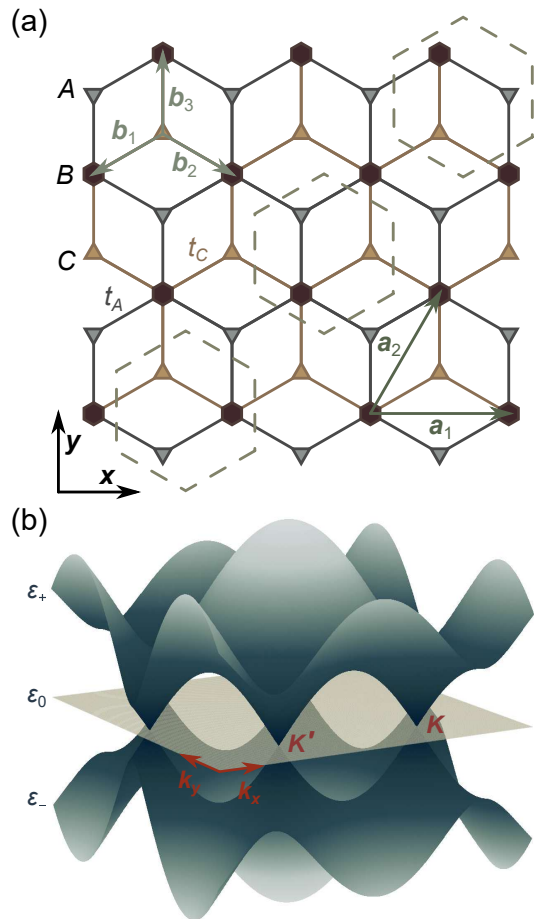


FIG. 5. (a) The α - T_3 lattice. The hopping parameter between the B and A (C) sites is t_A (t_C), with $t_C/t_A = \alpha \in [0, 1]$. The dashed hexagons indicate three choices to define the unit cell. \mathbf{b}_1 , \mathbf{b}_2 , and \mathbf{b}_3 are the nearest neighbor vectors. \mathbf{a}_1 and \mathbf{a}_2 are the primitive vectors. (b) Energy dispersion of the α - T_3 lattice, where ϵ_- , ϵ_0 , and ϵ_+ are the valence, flat, and conduction bands, respectively.

For $\alpha = 0$, the α - T_3 lattice reduces to graphene with a zero-energy flat band that originates from the uncoupled C sites.

Since $h(\mathbf{k})$ is scaled by t , the energy eigenvalues of Eq. (36) are independent of α as follows:

$$\epsilon_s(\mathbf{k}) = st \sqrt{1 + \beta^2(k_x) + 2\beta(k_x) \cos\left(\frac{\sqrt{3}}{2}k_y a\right)}, \quad (37a)$$

$$\epsilon_0 = 0, \quad (37b)$$

where $\beta(k_x) \equiv 2 \cos(k_x a/2) \geq 0$ for $k_x \in [-\pi/a, \pi/a]$. ϵ_s indicates the energy of the valence (conduction) band for $s = -1$ ($+1$). In addition, ϵ_0 appears due to the sublattice imbalance. In Fig. 5(b), the Dirac cones touch ϵ_0 at the \mathbf{K} and \mathbf{K}' points (labeled by $\tau = +1$ and -1 , respectively) in the corners of hexagonal BZ.

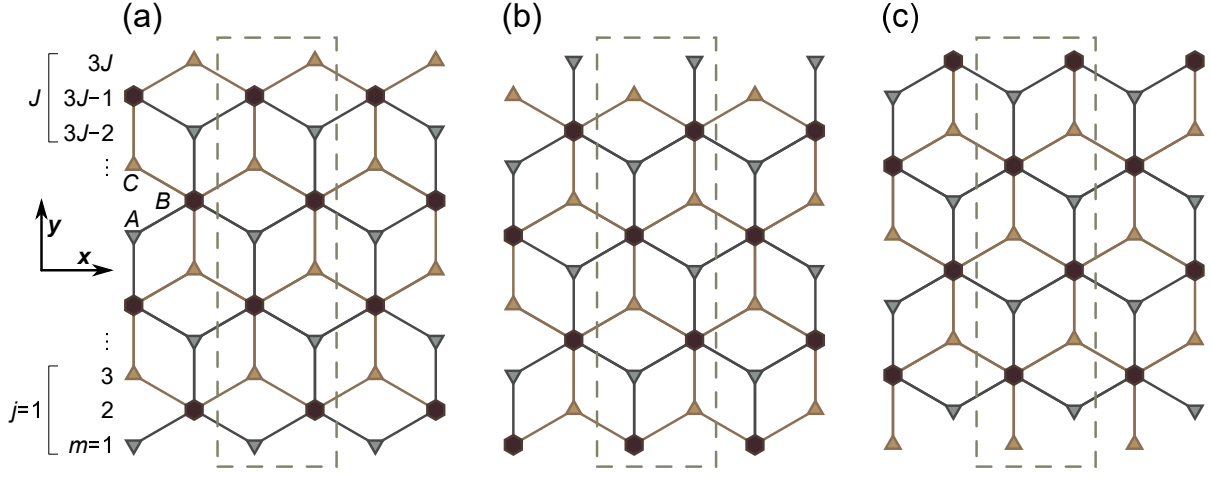


FIG. 6. The commensurate α - T_3 ZRs: (a) ABC (b) BCA and (c) CAB ZRs. In each supercell (dashed rectangle), the positions of site and trimer along the y axis are indicated by m and j , respectively.

The eigenvector of ε_s is given by

$$|\psi_s(\mathbf{k})\rangle = \frac{1}{\sqrt{2}} \begin{bmatrix} \cos \vartheta e^{-i\varphi(\mathbf{k})} \\ s \\ \sin \vartheta e^{i\varphi(\mathbf{k})} \end{bmatrix}. \quad (38a)$$

As for ε_0 , we get

$$|\psi_0(\mathbf{k})\rangle = \begin{bmatrix} \sin \vartheta e^{-i\varphi(\mathbf{k})} \\ 0 \\ -\cos \vartheta e^{i\varphi(\mathbf{k})} \end{bmatrix}. \quad (38b)$$

The Berry phase $\Gamma_c \equiv i \oint d\mathbf{k} \cdot \langle \psi_c(\mathbf{k}) | \nabla_{\mathbf{k}} | \psi_c(\mathbf{k}) \rangle$ can be analytically evaluated by contour integration along a path enclosing each Dirac point, as follows [48]:

$$\Gamma_{s,\tau} = \pi\tau \cos(2\vartheta), \quad (39a)$$

$$\Gamma_{0,\tau} = -2\pi\tau \cos(2\vartheta). \quad (39b)$$

Thus, $\Gamma_c \neq \pi$ or $0 \pmod{2\pi}$ for $\alpha \neq 0$ or 1 . Furthermore, Γ_c 's possess opposite signs for the K and K' valleys except for $\alpha = 0$ and 1 .

IV. α - T_3 ZRS

A. Types of ZR

Fig. 6 illustrates commensurate α - T_3 ZRs that we call (a) ABC, (b) BCA, and (c) CAB ZRs. The ZRs are respectively constructed by translating the bottom, middle, and top unit cells in Fig. 5(a) along the x direction with the periodicity \mathbf{a}_1 . The width of the ZR is characterized by a positive integer J , which is the number of trimers in the supercell (dashed rectangle). Starting from the bottom edge, the indices $m = 1, 2, \dots, 3J$ and $j = 1, 2, \dots, J$ specify the positions of sites and trimers, respectively,

in the y axis. Additionally, we can construct two non-commensurate ZRs from each commensurate ZR. First, by eliminating the sites at $m = 3J$, and second, by eliminating the sites at $m = 3J$ and $m = 3J - 1$. Therefore, there are nine types of α - T_3 ZRS: three commensurate and six non-commensurate ZRs.

Here, we will discuss the BBCs for the BCA and CAB ZRs. The existence of edge states in the ABC ZR is discussed in Appendix A.

B. Open boundary conditions for ZRs

In an infinite system, the TBES with nearest-neighbor interactions at the A , B , C sites are given by

$$\varepsilon \psi_s^A(\mathbf{r}) = -t_A \sum_{n=1}^3 \psi_s^B(\mathbf{r} - \mathbf{b}_n), \quad (40)$$

$$\varepsilon \psi_s^B(\mathbf{r}) = -\sum_{n=1}^3 [t_A \psi_s^A(\mathbf{r} + \mathbf{b}_n) + t_C \psi_s^C(\mathbf{r} - \mathbf{b}_n)], \quad (41)$$

$$\varepsilon \psi_s^C(\mathbf{r}) = -t_C \sum_{n=1}^3 \psi_s^B(\mathbf{r} + \mathbf{b}_n), \quad (42)$$

respectively. The missing terms of TBES on the edges of ZRs constitute the boundary conditions. The wavefunction $\psi_s = (\psi_s^A \ \psi_s^B \ \psi_s^C)^T$ is given by a linear combination of the Bloch states [11]:

$$\psi_s(\mathbf{r}) \equiv \mathcal{A} e^{i\mathbf{k}\cdot\mathbf{r}} |\psi_s(\mathbf{k})\rangle + \mathcal{A}' e^{i\mathbf{k}'\cdot\mathbf{r}} |\psi_s(\mathbf{k}')\rangle. \quad (43)$$

The amplitudes \mathcal{A} and \mathcal{A}' , and momenta \mathbf{k} and \mathbf{k}' are determined to satisfy the boundary conditions.

1. BCA ZR

In Fig. 7(a), the vector $\mathbf{L} = (L_x, L_y)$ connects an empty A site at $m = 0$ to an empty B site at $m = 3J + 1$ chosen as the origin $\mathbf{O} = (0, 0)$. $L_x = 0$ and $-a/2$ for odd and even J , respectively, while

$$L_y = \rho - \frac{a}{\sqrt{3}}, \text{ with } \rho \equiv \frac{\sqrt{3}}{2}(J+1)a. \quad (44)$$

Let us define $\mathbf{L}_l \equiv \mathbf{L} + l\mathbf{a}$ and $\mathbf{O}_l \equiv \mathbf{O} + l\mathbf{a}$, for $l \in \mathbb{Z}$. Thus, $\mathbf{L}_0 = \mathbf{L}$ and $\mathbf{O}_0 = \mathbf{O}$. Consider the TBEs at $m = 1$ and $m = 3J$ where $\mathbf{r} = -\mathbf{L}_l - \mathbf{b}_2$ and $\mathbf{r} = -\mathbf{O}_l + \mathbf{b}_1$, respectively, as follows:

$$\begin{aligned} \varepsilon\psi_s^B(-\mathbf{L}_l - \mathbf{b}_2) &= -t_C\psi_s^C(-\mathbf{L}_l + \mathbf{b}_3) \\ &\quad - t_C\psi_s^C(-\mathbf{L}_{l+1} + \mathbf{b}_3) \\ &\quad - t_A\psi_s^A(-\mathbf{L}_{l+1} + \mathbf{a}_2), \end{aligned} \quad (45)$$

$$\varepsilon\psi_s^A(-\mathbf{O}_l + \mathbf{b}_1) = -t_A\psi_s^B(-\mathbf{O}_l - \mathbf{a}_2). \quad (46)$$

The boundary conditions are thus given by

$$\begin{aligned} \psi_s^A(-\mathbf{L} - l\mathbf{a}_1) + \psi_s^A(-\mathbf{L} - [l+1]\mathbf{a}_1) \\ + \alpha\psi_s^C(-\mathbf{L} - l\mathbf{a}_1 + \mathbf{b}_1) = 0, \end{aligned} \quad (47)$$

$$\psi_s^B(-l\mathbf{a}_1) = 0. \quad (48)$$

2. CBA ZR

Fig. 7(b) shows that \mathbf{O} is assigned to an empty B site at $m = 0$. The TBEs at $m = 1$ and $m = 3J$ are

$$\varepsilon\psi_s^C(\mathbf{O}_l - \mathbf{b}_2) = -t_C\psi_s^B(\mathbf{O}_{l-1} + \mathbf{a}_2), \quad (49)$$

$$\begin{aligned} \varepsilon\psi_s^B(\mathbf{L}_l + \mathbf{b}_1) &= -t_A\psi_s^A(\mathbf{L}_l - \mathbf{b}_3) \\ &\quad - t_A\psi_s^A(\mathbf{L}_{l-1} - \mathbf{b}_3) \\ &\quad - t_C\psi_s^C(\mathbf{L}_l - \mathbf{a}_2). \end{aligned} \quad (50)$$

The boundary conditions given as follows:

$$\psi_s^B(l\mathbf{a}_1) = 0, \quad (51)$$

$$\begin{aligned} \alpha \{ \psi_s^C(\mathbf{L} + l\mathbf{a}_1) + \psi_s^C(\mathbf{L} + [l-1]\mathbf{a}_1) \} \\ + \psi_s^A(\mathbf{L} + l\mathbf{a}_1 - \mathbf{b}_2) = 0. \end{aligned} \quad (52)$$

C. The existence of edge states in ZRs

1. BCA ZR

In Appendix B 1, we show in detail that by combining Eqs. (47) and (48), we obtain

$$e^{-ik_y\rho} f_1^*(\mathbf{k}) = e^{ik_y\rho} f_1(\mathbf{k}). \quad (53)$$

Here, $f_1(\mathbf{k}) = |f_1(\mathbf{k})|e^{-i\phi_1(\mathbf{k})}$ is defined by

$$f_1(\mathbf{k}) \equiv v_A(k_x) + v'_{A1}(k_x)e^{-i\frac{\sqrt{3}}{2}k_y a}, \quad (54)$$

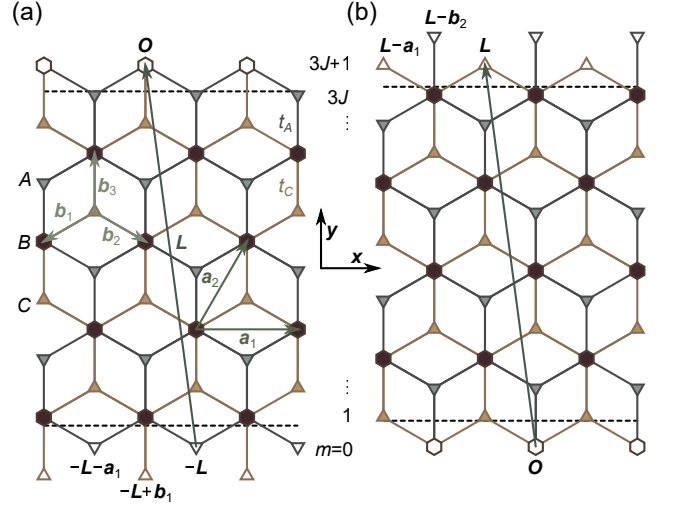


FIG. 7. Schematics for the boundary conditions of (a) BCA and (b) CAB ZRs.

where $v_A(k_x)$ and $v'_{A1}(k_x)$ depend on $\beta(k_x)$ as follows:

$$v_A \equiv \beta(1 + \alpha^2), \quad (55)$$

$$v'_{A1} \equiv \alpha^2 + \beta^2. \quad (56)$$

It is clear that $\phi_1(k_x, 2\pi/\sqrt{3}a) = \pi$ and 0 for $v_A/v'_{A1} < 1$ and $v_A/v'_{A1} > 1$, respectively. The quantization condition of the bulk states is therefore given by

$$\frac{\sqrt{3}}{2}(J+1)k_y a - \phi_1(\mathbf{k}) = n\pi, \text{ for } n = 1, \dots, J. \quad (57)$$

The intersections of $\phi_1(\mathbf{k})$ and $l'_n(k_y) \equiv \sqrt{3}(J+1)k_y a/2 - n\pi$ along $k_y \in (0, 2\pi/\sqrt{3}a)$ gives the solutions of Eq. (57). As discussed in Sec. II, a pair of bulk states become edge states when $(v_A/v'_{A1})_J < 1 - 1/(J+1)$, or in terms of β :

$$\beta^2 - \frac{1 + \alpha^2}{1 - (J+1)^{-1}}\beta + \alpha^2 > 0. \quad (58)$$

For $\alpha \neq 0$, Eq. (58) possesses two solutions: $\beta_J^+ < \beta \leq 2$ or $0 \leq \beta < \beta_J^-$, where $\beta_J^\pm \equiv 2 \cos(\chi_J^\pm a/2)$. Thus, χ_J^\pm correspond to $|k_x|$'s at which the transitions from bulk to edge states occur. The edge states exist in the range

$$0 \leq |k_x| < \chi_J^+ \text{ and } \chi_J^- < |k_x| \leq \pi/a. \quad (59)$$

In the limit $J \rightarrow \infty$, χ_J^\pm converge to

$$\chi_\infty^+ \sim (2/a) \cos^{-1}(1/2) = 2\pi/3a, \quad (60a)$$

$$\chi_\infty^- \sim (2/a) \cos^{-1}(\alpha^2/2). \quad (60b)$$

Thus, apart from the Dirac point χ_∞^+ , the bulk states undergo transition to edge states at χ_∞^- for $\alpha \in (0, 1)$.

Let $1/\kappa_y$ be the localization length of edge states. By substituting $k_y = 2\pi/\sqrt{3}a + i\kappa_y$ into Eqs. (53) and (54),

$$e^{\kappa_y\rho} \tilde{f}_1(-\kappa_y) = e^{-\kappa_y\rho} \tilde{f}_1(\kappa_y), \quad (61)$$

where we define

$$\tilde{f}_1(\kappa_y) \equiv v_A(k_x) - v'_{A1}(k_x)e^{\frac{\sqrt{3}}{2}\kappa_y a}. \quad (62)$$

Therefore, κ_y is computed by solving

$$\delta_1(\kappa_y) \equiv \frac{v_A}{v'_{A1}} - \frac{\sinh(\sqrt{3}J\kappa_y a/2)}{\sinh(\rho\kappa_y)} = 0. \quad (63)$$

Analytically, the energies of edge states are calculated by inserting $k_y = 2\pi/\sqrt{3}a + i\kappa_y$ into Eq. (37a) as follows:

$$\tilde{\varepsilon}_s(\kappa_y) = st\sqrt{1 + \beta^2 - 2\beta\cosh\left(\frac{\sqrt{3}}{2}\kappa_y a\right)}. \quad (64)$$

By substituting Eq. (63) into (64), $\tilde{\varepsilon}_s$ for $J\kappa_y a \gg 1$ is

$$\tilde{\varepsilon}_s = st\frac{\alpha|1 - \beta^2|}{\sqrt{1 + \alpha^2}\sqrt{\alpha^2 + \beta^2}}. \quad (65)$$

Since β depends on k_x , $\tilde{\varepsilon}_s$ is dispersive. In particular, we get $\tilde{\varepsilon}_s \approx 0$ and $\tilde{\varepsilon}_s = st_A$ at $|k_x| \approx 2\pi/3a$ and $|k_x| = \pi/a$, respectively. Thus, the ZR is gapless for $J \rightarrow \infty$.

Fig. 8(a) depicts the numerical calculation of energy spectra as function of k_x for $\alpha = 0.8$ and $J = 20$. By solving Eq. (58), we get $\chi_{20}^+ \approx 0.5985\pi/a$ and $\chi_{20}^- \approx 0.8251\pi/a$, which are indicated by the vertical dashed and dotted lines, respectively (we check that χ_J^+ is undefined for $J < 3$). The bold red lines depict the edge states, which are pinned at $|\varepsilon| = t_A \approx 0.7809t$ at $|k_x| = \pi/a$, in agreement with Eq. (65). Due to the finite size effect, band gaps open at $|k_x| = 2\pi/3a$.

In Figs. 8(b)-(e), we plot the electronic probability density $|\psi|^2$ for the in-gap states per site m at several k_x 's. It is noted that $|\psi|^2$'s are identical for both signs of k_x and ε . The grey, brown, and yellow bars in the histogram correspond to the A, B, and C sites, respectively. The distributions of $|\psi|^2$ in Figs. 8(b) and (c) exhibit the profiles of asymmetric edge states. Here, $|\psi|^2$'s are concentrated around the bottom edge of the ZR and decay exponentially towards the top edge. Figs. 8(d) and (e) indicate the bulk state because $|\psi|^2$'s are extended throughout the ZR. In Fig. 8(e), $|\psi|^2$ is high around the bottom edge because k_x is close to χ_{20}^- . The inset shows the re-emergence of the edge state at a larger k_x .

2. CAB ZR

In Appendix B 2, we show in detail that Eqs. (51) and (52) lead to:

$$e^{ik_y \rho} f_2(\mathbf{k}) = e^{-ik_y \rho} f_2^*(\mathbf{k}), \quad (66)$$

where $f_2(\mathbf{k}) = |f_2(\mathbf{k})|e^{-i\phi_2(\mathbf{k})}$ is defined by

$$f_2(\mathbf{k}) \equiv v_A(k_x) + v'_{A2}(k_x)e^{-i\frac{\sqrt{3}}{2}k_y a}, \quad (67)$$

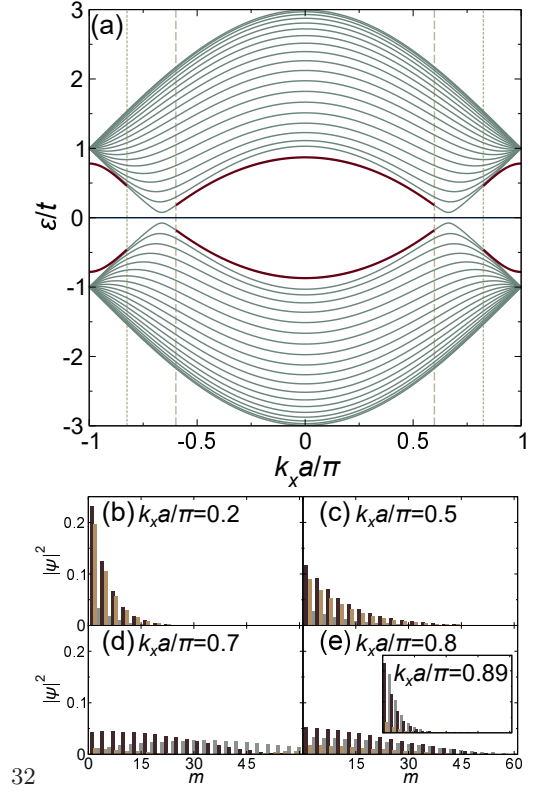


FIG. 8. (a) Energy spectra of the BCA ZR as a function of k_x for $\alpha = 0.8$ and $J = 20$. The bold red lines indicate the edge states. The blue line at $\varepsilon = 0$ is the flat band. The transitions from bulk to edge states occur at $|k_x| \approx 0.5985\pi/a$ and $0.8251\pi/a$, accordingly marked by the vertical dashed and dotted lines. Probability density for the in-gap states per site m at (b) $k_x = 0.2\pi/a$, (c) $0.5\pi/a$, (d) $0.7\pi/a$, and (e) $0.8\pi/a$ (Inset: $0.89\pi/a$). The grey, brown, and yellow bars correspond to the A, B, and C sites, respectively.

and $v'_{A2}(k_x)$ is given as follows:

$$v'_{A2} \equiv (1 + \alpha^2\beta^2). \quad (68)$$

The quantization condition of k_y is given by replacing ϕ_1 in Eq. (57) with ϕ_2 . Likewise, edge states appear in the gap when $(v_A/v'_{A2})J < 1 - 1/(J+1)$, or

$$\alpha^2\beta^2 - \frac{1 + \alpha^2}{1 - (J+1)^{-1}}\beta + 1 > 0. \quad (69)$$

By denoting the solutions of Eq. (69) as $\beta_J^+ < \beta \leq 2$ or $0 \leq \beta < \beta_J^-$, the edge states for $\alpha \neq 0$ exist in the range

$$0 \leq |k_x| < \chi_J^+ \text{ and } \chi_J^- < |k_x| \leq \pi/a. \quad (70)$$

Note that χ_J^\pm in Eq. (70) are not equal to those in Eq. (59) except for $\alpha = 1$. Here, in the limit $J \rightarrow \infty$, χ_J^\pm become

$$\chi_\infty^+ \sim (2/a) \cos^{-1}(1/2\alpha^2), \quad (71a)$$

$$\chi_\infty^- \sim (2/a) \cos^{-1}(1/2) = 2\pi/3a. \quad (71b)$$

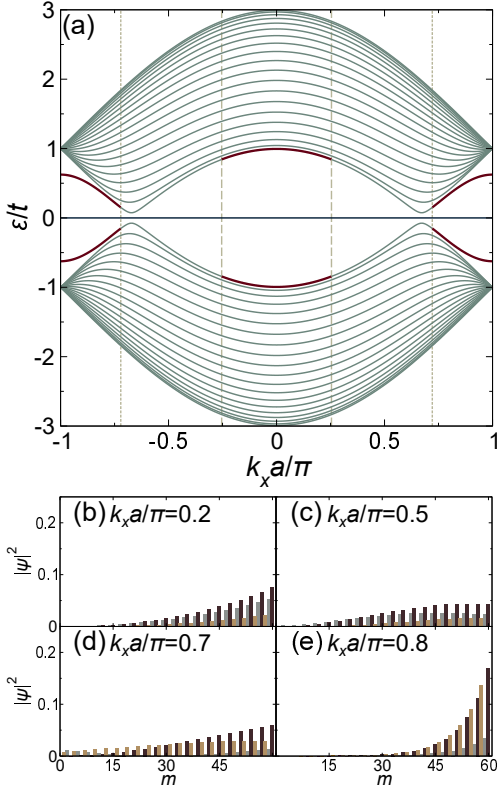


FIG. 9. (a) Energy spectra ε of the CAB ZR as a function of k_x for $\alpha = 0.8$ and $J = 20$. The bold red lines indicate the edge states. The blue line at $\varepsilon = 0$ is the flat band. The transitions from bulk to edge states occur at $|k_x| \approx 0.2542\pi/a$ and $0.7213\pi/a$, accordingly marked by the vertical dashed and dotted lines. Probability density for the in-gap states per site m at (b) $k_x = 0.2\pi/a$, (c) $0.5\pi/a$, (d) $0.7\pi/a$, and (e) $0.8\pi/a$. The grey, brown, and yellow bars correspond to the A, B, and C sites, respectively.

It is noticed that χ_∞^\pm is undefined for $\alpha < 1/\sqrt{2}$.

To determine κ_y , we define δ_2 by replacing v'_{A1} in Eq. (63) with v'_{A2} . $\tilde{\varepsilon}_s$ for $J\kappa_y a \gg 1$ is given by

$$\tilde{\varepsilon}_s = st \frac{\alpha |1 - \beta^2|}{\sqrt{1 + \alpha^2} \sqrt{1 + \alpha^2 \beta^2}}. \quad (72)$$

At $|k_x| \approx 2\pi/3a$ ($|k_x| = \pi/a$), $\tilde{\varepsilon}_s \approx 0$ ($\tilde{\varepsilon}_s = st_C$).

Fig. 9(a) shows the numerical calculation of energy spectra as a function of k_x for $\alpha = 0.8$ and $J = 20$. By solving Eq. (69), $\chi_{20}^+ \approx 0.2542\pi/a$ and $\chi_{20}^- \approx 0.7213\pi/a$, respectively marked by the vertical dashed and dotted lines (χ_J^\pm is undefined for $J < 12$). The bold red lines indicate the edge states, where $|\varepsilon| = t_C \approx 0.6247t$ at $|k_x| = \pi/a$, in accordance with Eq. (72).

Figs. 9(b)-(e) show $|\psi|^2$'s for the in-gap states per site m at several k_x 's. Figs. 9(b) and (e) exhibit the profiles of asymmetric edge states where $|\psi|^2$'s are high around the top edge of ZR and decay exponentially toward the bottom edge. In contrast, Figs. 9(c) and (d) indicate the bulk states due to the extended $|\psi|^2$'s.

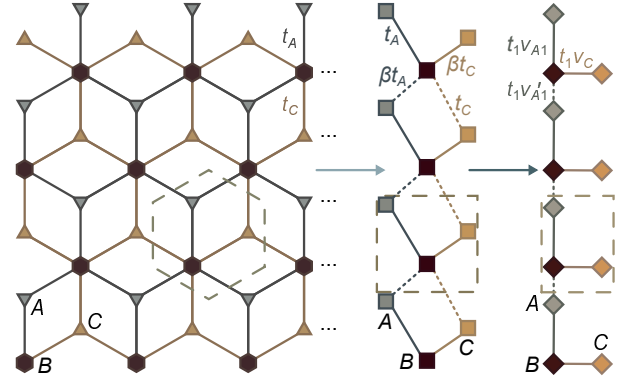


FIG. 10. Schematic for the mappings of BCA ZR into rhombic and stub SSH chains.

V. TOPOLOGICAL INVARIANT OF α - T_3 ZRS

A. Unitary transforms of bulk Hamiltonian

In Section IV, we found that for each k_x , the α - T_3 ZRs are isomorphic to the stub SSH chain along the y direction. By unitary transforms of $h(\mathbf{k})$ in Eq. (34), the BCA and CAB ZRs are mapped into stub SSH chains with distinct unit cells and hopping parameters. As a result, the \mathbb{Z}_2 invariant for the α - T_3 ZRs is given by $|W_c|$.

1. BCA ZR

To transform $h(\mathbf{k})$, we define a unitary matrix

$$U(\mathbf{u}_A, \mathbf{u}_C) \equiv \begin{bmatrix} e^{i\mathbf{k} \cdot \mathbf{u}_A} & 0 & 0 \\ 0 & 1 & 0 \\ 0 & 0 & e^{i\mathbf{k} \cdot \mathbf{u}_C} \end{bmatrix}. \quad (73)$$

$h_1(\mathbf{k}) \equiv U(\mathbf{b}_3, -\mathbf{b}_1 - \frac{\mathbf{a}_1}{2})h(\mathbf{k})U^\dagger(\mathbf{b}_3, -\mathbf{b}_1 - \frac{\mathbf{a}_1}{2})$ is

$$h_1(\mathbf{k}) = - \begin{bmatrix} 0 & t_A p^*(\mathbf{k}) & 0 \\ t_A p(\mathbf{k}) & 0 & t_C q(\mathbf{k}) \\ 0 & t_C q^*(\mathbf{k}) & 0 \end{bmatrix}, \quad (74)$$

where we define

$$p(\mathbf{k}) \equiv 1 + \beta(k_x) e^{-i\frac{\sqrt{3}}{2}k_y a}, \quad (75)$$

$$q(\mathbf{k}) \equiv \beta(k_x) + e^{-i\frac{\sqrt{3}}{2}k_y a}. \quad (76)$$

$h_1(\mathbf{k})$ is the Hamiltonian of a rhombic or diamond chain [109–111] illustrated in the middle panel of Fig. 10. Here, the A and C sites are connected to the B sites by the intracell (intercell) hopping parameters t_A and βt_C (βt_A and t_C), respectively. Experimental realizations of the rhombic chain have been achieved using photonic lattices [109, 110]. The present method is therefore applicable for topological characterization of edge states [111] in the rhombic chains.

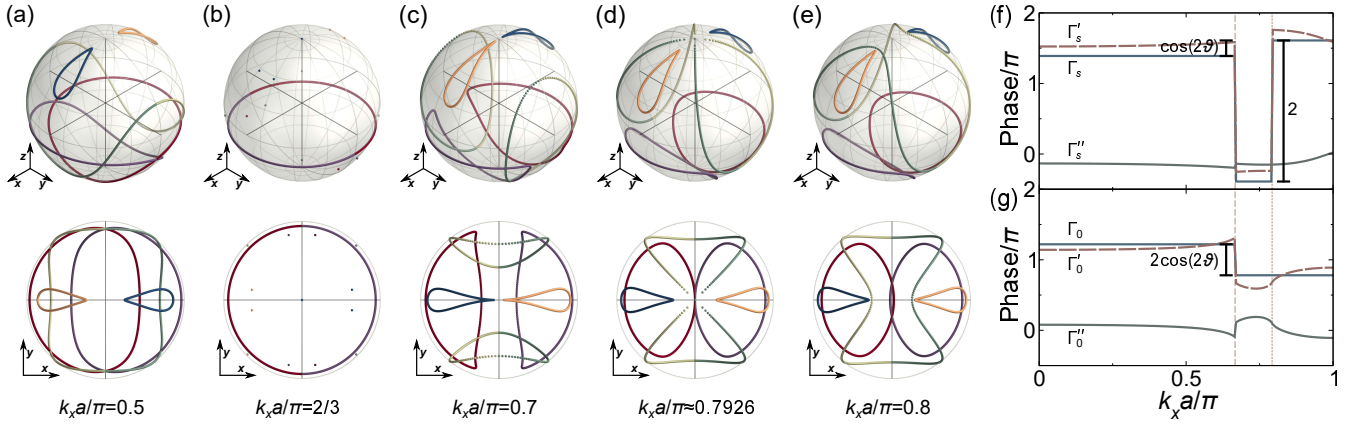


FIG. 11. Trajectories of the Majorana stars [from the eigenstates of $\mathcal{H}_1(\mathbf{k})$, with $\alpha = 0.8$] on the Bloch sphere (top panels) and the xy plane (bottom panels) at (a) $k_x = 0.5\pi/a$, (b) $\chi_\infty^+ = 2\pi/3a$ [Eq. (60a)] (c) $0.7\pi/a$, (d) $\chi_\infty^- \approx 0.7926\pi/a$ [Eq. (60b)], and (e) $0.8\pi/a$. The red and yellow (blue and purple) curves correspond to the valence (conduction) band, $c = -1$ ($c = +1$). The light- and dark-green curves correspond to the flat band, $c = 0$. Plots of Γ_c , Γ'_c , and Γ''_c for (f) $c = s = \pm 1$, (g) $c = 0$.

Now, consider a rotation matrix

$$\Upsilon(\gamma_1) \equiv \begin{bmatrix} \cos \gamma_1 & 0 & \sin \gamma_1 \\ 0 & 1 & 0 \\ -\sin \gamma_1 & 0 & \cos \gamma_1 \end{bmatrix}. \quad (77)$$

By setting $\gamma_1 = \tan^{-1}(\alpha/\beta)$, we transform h_1 into $\mathcal{H}_1(\mathbf{k}) = \Upsilon(\gamma_1)h_1(\mathbf{k})\Upsilon^\dagger(\gamma_1)$ as follows:

$$\mathcal{H}_1(\mathbf{k}) = -t_1 \begin{bmatrix} 0 & f_1^*(\mathbf{k}) & 0 \\ f_1(\mathbf{k}) & 0 & -v_C \\ 0 & -v_C & 0 \end{bmatrix}, \quad (78)$$

where $t_1 \equiv t_A \cos \gamma_1 / \beta$, $v_C \equiv \alpha(1 - \beta^2)$, and $f_1(\mathbf{k})$ is defined by Eq. (54). $\mathcal{H}_1(\mathbf{k})$ constitutes the Hamiltonian of stub SSH chain illustrated in the right panel of Fig. 10. The mapping of $h(\mathbf{k})$ into $\mathcal{H}_1(\mathbf{k})$ explains the emergence edge states with energies $\tilde{\epsilon}_s = s|t_1 v_C|$, identical to Eq. (65), when $v_A/v'_A < 1$.

The eigenstates of $\mathcal{H}_1(\mathbf{k})$ are derived by replacing $\Phi(k)$ and $\Theta(k)$ in see Eqs. (7a), (7b) with $\phi_1(\mathbf{k})$ and $\theta_1(\mathbf{k}) \equiv \tan^{-1}(-v_C(k_x)/|f(\mathbf{k})|)$, respectively. Here, the BZ is $k_y \in [-2\pi/\sqrt{3}a, 2\pi/\sqrt{3}a]$. ζ_c^ν and $|W_c|$ are calculated by using the method discussed in Sec. II.

Fig. 11 shows the trajectories of ζ_c^ν 's for $\alpha = 0.8$ at (a) $k_x = 0.5\pi/a$, (b) $\chi_\infty^+ = 2\pi/3a$ [K point, see Eq. (60a)], (c) $0.7\pi/a$, (d) $\chi_\infty^- \approx 0.7926\pi/a$ [see Eq. (60b)], and (e) $0.8\pi/a$. The red/yellow, light-green/dark-green, and blue/purple curves correspond to $c = -1$, 0 , and 1 , respectively. In Figs. 11(a) and (e), $|W_c| = 1$ because $0 < k_x < \chi_\infty^+$ and $\chi_\infty^- < k_x < \pi/a$, respectively. In Fig. 11(c), $|W_c| = 0$ because $\chi_\infty^+ < k_x < \chi_\infty^-$. W_c 's are ill-defined at χ_∞^\pm for different reasons. In Fig. 11(b), the trajectories of ζ_c^ν 's become discontinuous due to the gap closing at $|k_y| = 2\pi/\sqrt{3}a$. Here, the system is reduced to the metallic SSH chain because $\beta = 1$ and consequently $v_C = 0$, $v_A = v'_A$. In Fig. 11(d), the red, purple, and connected green curves intersect the poles of the Bloch

sphere. Accordingly, Figs. 11(b) and (d) indicate topological phase transitions with and without gap closing.

To show that the unitary transforms preserve the topological properties of the α - T_3 ZR, we numerically compute the accumulated Berry phase Γ_c from the adiabatic evolution of ζ_c^ν 's. For $S = 1$, Γ_c is given by [99, 100]:

$$\Gamma_c = \Gamma'_c + \Gamma''_c, \quad \text{where} \quad (79)$$

$$\Gamma'_c \equiv -\frac{1}{2} \sum_{\nu=\mp} \int_{\text{BZ}} (1 - \cos \eta_c^\nu) d\zeta_c^\nu, \quad (80)$$

$$\Gamma''_c \equiv -\frac{1}{2} \int_{\text{BZ}} \frac{\zeta_c^- \times \zeta_c^+}{3 + \zeta_c^- \cdot \zeta_c^+} \cdot d(\zeta_c^- - \zeta_c^+). \quad (81)$$

Γ'_c corresponds to the sum of solid angles subtended by ζ_c^- and ζ_c^+ , while Γ''_c is interpreted as the correlation term between ζ_c^- and ζ_c^+ due to their relative motions.

Fig. 11(f) shows Γ_s , Γ'_s , and Γ''_s as a function of k_x , where the vertical dashed and dotted lines mark $k_x = \chi_\infty^+$ and χ_∞^- , respectively. It is noted that Γ'_s , Γ''_s and hence Γ_s are identical for $s = \pm 1$. For $0 \leq k_x < \chi_\infty^+$, Γ'_s includes the large portion of the Bloch sphere bounded by the red (or purple) loop that encloses the z axis [see Fig. 11(a) for instance], where $\Gamma_s \approx 1.390244\pi$. The trajectories of ζ_s^ν 's become disconnected at χ_∞^+ [Fig. 11(b)] and reconnect for $\chi_\infty^+ < k_x \leq \chi_\infty^-$, where $\Gamma_s \approx -0.390244\pi$. The abrupt decrease of Γ_s is because Γ'_s comprises the small portion of the Bloch sphere as the red (or purple) loop does not enclose the z axis [Figs. 11(c) and (d) for examples]. For $\chi_\infty^- < k_x \leq \pi/a$, Γ_s increases by 2π to $\Gamma_s \approx 1.609756\pi$ as the red (or purple) loop re-encloses the z axis [see Figs. 11(e)]. Since Γ_s is defined modulo 2π , Γ_s can not distinguish between the trivial and non-trivial phases of the ZR for $\chi_\infty^+ < k_x < \chi_\infty^-$ and $\chi_\infty^- < k_x \leq \pi/a$, respectively. It is noted that Γ_s for $k_x \in (\chi_\infty^-, \pi/a)$ and $k_x \in [0, \chi_\infty^+)$ differs by $\pi \cos(2\vartheta) \approx 0.219512\pi \pmod{2\pi}$, consistent with Eq. (39a) for $\vartheta = \tan^{-1}(0.8)$ and $\tau = 1$.

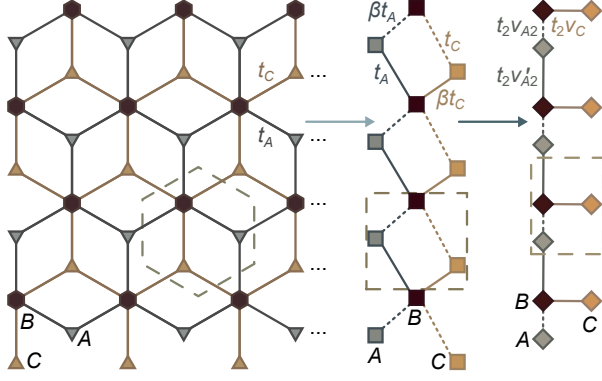


FIG. 12. Schematic for the mappings of CAB ZR into rhombic and stub SSH chains.

Fig. 11(g) shows Γ_0 , Γ'_0 , and Γ''_0 as a function of k_x . Γ'_0 either corresponds to a portion of the Bloch sphere bounded by a single loop [as in Figs. 11(a) and (e)], or two loops [as in Figs. 11(c) and (d)]. The jump discontinuity from $\Gamma_0 \approx 1.219512\pi$ to $\Gamma_0 \approx 0.780488\pi$ occurs at $k_x = \chi_{\infty}^+$. Therefore, Γ_0 for $k_x \in (\chi_{\infty}^+, \pi/a]$ and $k_x \in [0, \chi_{\infty}^+)$ differs by $-2\pi \cos(2\vartheta) \approx -0.439024\pi$, in agreement with Eq. (39b) for $\vartheta = \tan^{-1}(0.8)$ and $\tau = 1$.

2. CAB ZR

By using Eq. (73), we can transform $h(\mathbf{k})$ into $h_2(\mathbf{k}) \equiv U(\mathbf{b}_2 - \frac{\mathbf{a}_1}{2}, -\mathbf{b}_3)h(\mathbf{k})U^\dagger(\mathbf{b}_2 - \frac{\mathbf{a}_1}{2}, -\mathbf{b}_3)$ as follows:

$$h_2(\mathbf{k}) = - \begin{bmatrix} 0 & t_A q(\mathbf{k}) & 0 \\ t_A q^*(\mathbf{k}) & 0 & t_C p^*(\mathbf{k}) \\ 0 & t_C p(\mathbf{k}) & 0 \end{bmatrix}. \quad (82)$$

The middle panel of Fig. 12 shows the system described by Eq. (82), which is a rhombic chain with a distinct choice of unit cell compared with the one in Fig. 10.

By using Υ in Eq. (77), $h_2(\mathbf{k})$ is transformed into $\mathcal{H}_2(\mathbf{k}) = \Upsilon(\gamma_2)h_2(\mathbf{k})\Upsilon^\dagger(\gamma_2)$ as follows:

$$\mathcal{H}_2(\mathbf{k}) = -t_2 \begin{bmatrix} 0 & f_2(\mathbf{k}) & 0 \\ f_2^*(\mathbf{k}) & 0 & v_C \\ 0 & v_C & 0 \end{bmatrix}, \quad (83)$$

where $\gamma_2 \equiv \tan^{-1}(\alpha\beta)$, $t_2 \equiv t_A \cos \gamma_2$, and $f_2(\mathbf{k})$ is defined by Eq. (67). The right panel of Fig. 12 depicts the stub SSH chain represented by Eq. (83). Thus, edge states with energies $\tilde{\epsilon}_s = s|t_2 v_C|$ [identical to Eq. (72)] appear when for $v_A/v'_{A2} < 1$.

Similarly, we derive the eigenstates of $\mathcal{H}_2(\mathbf{k})$ by replacing $\Phi(k)$ and $\Theta(k)$ in Eqs. (7a), (7b) with $\phi_2(\mathbf{k})$ and $\theta_2(\mathbf{k}) = -\theta_1(\mathbf{k})$, respectively.

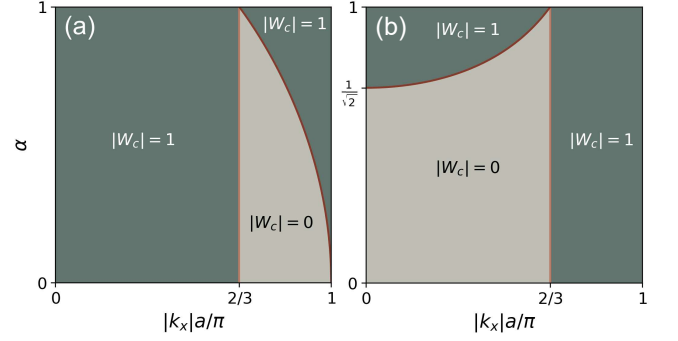


FIG. 13. Topological phase diagrams of (a) BCA and (b) CAB ZRs. The light (dark) region indicates the trivial (non-trivial) phase, where edge states are absent (present). The pink (red) lines mark the phase transition with (without) gap closing.

B. Topological phase diagrams of ZRs

Having shown that the distinction between the trivial and nontrivial phases of the α - T_3 ZRs is indicated by $|W_c|$, we discuss the topological phase diagrams as a function $|k_x| \in [0, \pi/a]$ and $\alpha \in [0, 1]$.

1. BCA ZR

Fig. 13(a) depicts the topological phase diagram of the BCA ZR. The light and dark regions indicate the trivial and nontrivial phases, respectively. The pink and red lines mark the phase transition with and without gap closing. For $\alpha = 0$, the edge states exist in the range $|k_x| \in [0, 2\pi/3a)$. This result is expected because removing the C sites reduces the BCA ZR to bearded graphene ribbons [11, 16], i.e. ZR with dangling bonds or the Klein defects. For $\alpha = 1$ (T_3 ZR), the edge states exist for $|k_x| \in [0, \pi/a]$ except at $|k_x| = 2\pi/3a$, even though the Berry phase $\Gamma_s = 0$. In the Majorana representation of the corresponding stub SSH chain, $|W_c| = 1$ before and after gap closing because $\chi_{\infty}^+ = \chi_{\infty}^- = 2\pi/3a$. Thus, when we plot Γ_s as a function of k_x , the value of Γ_s remains the same for $|k_x| \in [0, 2\pi/3a)$ and $(2\pi/3a, \pi/a]$.

2. CAB ZR

Fig. 13(b) shows the topological phase diagram of the CAB ZR. For $\alpha < 1/\sqrt{2}$, the edge states appear in the range $|k_x| \in (2\pi/3a, \pi/a]$, similar to those in the graphene ZR [11, 16, 106].

VI. CONCLUSION

In the first part of this paper, we investigate the bulk-boundary correspondence for the stub SSH chain. The

edge states appear when the intracell hopping parameter is smaller than the intercell one, identical to the SSH chain. By using the Majorana representation of the eigenstates on the Bloch sphere, we prove that the \mathbb{Z}_2 topological invariant is given by the winding number instead of the Zak phase, which is not quantized to π or 0 due to the broken inversion symmetry.

In the second part, we demonstrate the isomorphism between the α - T_3 ZRs and the stub SSH chains from the boundary conditions of the former. The equivalence between the two systems is revealed by the unitary transforms of the bulk Hamiltonian, which maps the α - T_3 ZRs into stub SSH chains. As a result, the edge states in the α - T_3 ZRs possess the same topological origin and characterization as those in the stub SSH chains. Therefore, the α - T_3 lattice is identified as a topologically non-trivial, massless Dirac fermion in two dimensions without a quantized Berry phase. The T_3 lattice particularly exemplifies a topological system with zero Berry phase.

ACKNOWLEDGMENT

We thank R. Saito, N. T. Hung, S. Hayashi, and E. H. Hasdeo for helpful discussions. This work is partly supported by Grant-in-Aid for Scientific Research, JSPS KAKENHI (23K03293), and JST-CREST (JP-MJCR18T1).

APPENDIX A: ABC ZR

Here, we derive the quantization condition of the bulk states and prove the existence of two dispersive edge states for each $\varepsilon < 0$ and $\varepsilon > 0$. The topological characterization of the edge states is reserved for future work.

The boundary conditions are derived by expressing the nearest-neighbor interactions for the B sites in terms of the next-nearest-neighbor interactions. First, we multiply Eq. (41) by ε , then we substitute ψ_s^A and ψ_s^C by the right-hand sides of Eqs. (40) and (42), respectively. As a result, Eq. (41) becomes

$$\varepsilon^2 \psi_s^B(\mathbf{r}) = t^2 \left[\sum_{\nu=\pm} \left\{ \psi_s^B(\mathbf{r} + \nu \mathbf{a}_1) + \psi_s^B(\mathbf{r} + \nu \mathbf{a}_2) + \psi_s^B(\mathbf{r} + \nu[\mathbf{a}_2 - \mathbf{a}_1]) \right\} + 3\psi_s^B(\mathbf{r}) \right]. \quad (\text{A1})$$

In Fig. 14(a), we define a vector $\mathcal{L} = (\mathcal{L}_x, \mathcal{L}_y)$, where $\mathcal{L}_x = 0$ and $-a/2$ for odd and even J , respectively, while $\mathcal{L}_y = \sqrt{3}(J-1)a/2$. For each $l \in \mathbb{Z}$, the TBEs at $m = 2$

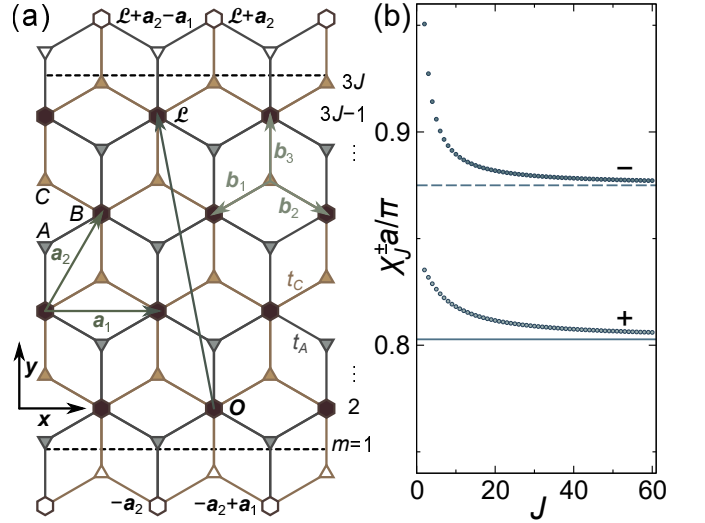


FIG. 14. ABC ZR: (a) Schematic for the boundary conditions. (b) Plot χ_J^\pm as a function of J for $\alpha = 0.8$. The solid and dashed lines mark $\chi_\infty^+ \approx 0.802769\pi/a$ and $\chi_\infty^- \approx 0.874979\pi/a$, respectively.

and $m = 3J - 1$ are accordingly given as follows:

$$\varepsilon \psi_s^B(\mathcal{O}_l) = -t_A \sum_{n=1}^3 \psi_s^A(\mathcal{O}_l + \mathbf{b}_n) - t_C \sum_{n=1}^2 \psi_s^C(\mathcal{O}_l - \mathbf{b}_n), \quad (\text{A2})$$

$$\varepsilon \psi_s^B(\mathcal{L}_l) = -t_A \sum_{n=1}^2 \psi_s^A(\mathcal{L}_l + \mathbf{b}_n) - t_C \sum_{n=1}^3 \psi_s^C(\mathcal{L}_l - \mathbf{b}_n). \quad (\text{A3})$$

We define $\mathcal{L}_l \equiv \mathcal{L} + l\mathbf{a}_1$ and $\mathcal{O}_l \equiv \mathcal{O} + l\mathbf{a}_1$, thus $\mathcal{L}_0 = \mathcal{L}$ and $\mathcal{O}_0 = \mathcal{O}$. By expressing ψ_s^A and ψ_s^C in terms of ψ_s^B , Eqs. (A2) and (A3) are respectively given by

$$\varepsilon^2 \psi_s^B(\mathcal{O}_l) = t_A^2 \psi_s^B(\mathcal{O}_l) + t^2 \left[2\psi_s^B(\mathcal{O}_l) + \psi_s^B(\mathcal{O}_l + \mathbf{a}_2) + \psi_s^B(\mathcal{O}_l + \mathbf{a}_2 - \mathbf{a}_1) + \sum_{\nu=\pm} \psi_s^B(\mathcal{O}_l + \nu \mathbf{a}_1) \right], \quad (\text{A4})$$

$$\varepsilon^2 \psi_s^B(\mathcal{L}_l) = t_C^2 \psi_s^B(\mathcal{L}_l) + t^2 \left[2\psi_s^B(\mathcal{L}_l) + \psi_s^B(\mathcal{L}_l - \mathbf{a}_2) + \psi_s^B(\mathcal{L}_l - \mathbf{a}_2 + \mathbf{a}_1) + \sum_{\nu=\pm} \psi_s^B(\mathcal{L}_l - \nu \mathbf{a}_1) \right]. \quad (\text{A5})$$

The missing terms of the TBEs at \mathcal{O}_l and \mathcal{L}_l constitute the boundary conditions as follows:

$$t_C^2 \psi_s^B(\mathcal{O}_l) + t^2 \left[\psi_s^B(\mathcal{O}_l - \mathbf{a}_2) + \psi_s^B(\mathcal{O}_l - \mathbf{a}_2 + \mathbf{a}_1) \right] = 0, \quad (\text{A6})$$

$$t_A^2 \psi_s^B(\mathcal{L}_l) + t^2 \left[\psi_s^B(\mathcal{L}_l + \mathbf{a}_2) + \psi_s^B(\mathcal{L}_l + \mathbf{a}_2 - \mathbf{a}_1) \right] = 0. \quad (\text{A7})$$

Therefore, the boundary conditions are not indeterminate as suggested by Ref. [112]. By adopting $\psi_s(\mathbf{r})$ in Eq. (43), and assuming $\mathbf{k}' = (k_x, -k_y)$ because momentum is conserved in the x direction, Eqs. (A6) and (A7) respectively reduce to

$$\mathcal{A}f_C(\mathbf{k}) + \mathcal{A}'f_C(\mathbf{k}') = 0, \quad (\text{A8})$$

$$\mathcal{A}e^{i\mathbf{k}\cdot\mathcal{L}}f_A(\mathbf{k}') + \mathcal{A}'e^{i\mathbf{k}'\cdot\mathcal{L}}f_A(\mathbf{k}) = 0, \quad (\text{A9})$$

where $f_\lambda(\mathbf{k}) = |f_\lambda(\mathbf{k})|e^{-i\phi_\lambda(\mathbf{k})}$, $\lambda = A, C$ are defined by

$$f_C(\mathbf{k}) \equiv \sin^2\vartheta + \beta(k_x)e^{-i\sqrt{3}k_y a/2}, \quad (\text{A10})$$

$$f_A(\mathbf{k}) \equiv \cos^2\vartheta + \beta(k_x)e^{-i\sqrt{3}k_y a/2}. \quad (\text{A11})$$

By combining Eqs. (A8) and (A9), we get

$$e^{ik_y\mathcal{L}_y}f_A(\mathbf{k}')f_C(\mathbf{k}') + e^{-ik_y\mathcal{L}_y}f_A(\mathbf{k})f_C(\mathbf{k}) = 0. \quad (\text{A12})$$

Thus, the quantization condition is derived as follows:

$$\frac{\sqrt{3}}{2}(J-1)k_y a + \phi_0(\mathbf{k}) = n\pi, \text{ for } n = 1, \dots, J, \quad (\text{A13})$$

where we define

$$\phi_0(\mathbf{k}) = \phi_A(\mathbf{k}) + \phi_C(\mathbf{k}). \quad (\text{A14})$$

Note that Eq. (A13) is not mathematically analogous to those of the BCA and CAB ZRs [see Eq. (57)].

By taking derivative of Eq. (A13) with respect to k_y and setting $k_y = 2\pi/\sqrt{3}a$, we obtain

$$\frac{J+1}{J-1}\beta^2 - \frac{J}{J-1}\beta + \frac{1}{4}\sin^2(2\vartheta) = 0, \text{ for } J \geq 2. \quad (\text{A15})$$

Similarly, the solutions of Eq. (A15) are denoted by $\beta_\pm^\pm = 2\cos(\chi_J^\pm/2)$. χ_J^\pm converge to

$$\chi_\infty^+ \sim (2/a)\cos^{-1}(\cos^2\vartheta/2), \quad (\text{A16a})$$

$$\chi_\infty^- \sim (2/a)\cos^{-1}(\sin^2\vartheta/2). \quad (\text{A16b})$$

Except for $\alpha = 0$, the transitions from bulk to edge states do not occur at $|k_x| = 2\pi/3a$, unlike the BCA and CAB ZRs. Fig. 14(b) shows χ_J^\pm as a function of $J = 2, \dots, 60$ for $\alpha = 0.8$. The solid and dashed lines indicate $\chi_\infty^+ \approx 0.80277\pi/a$ and $\chi_\infty^- \approx 0.87498\pi/a$, respectively.

Fig. 15(a) shows $\phi_0(\mathbf{k})$ for several k_x 's and $-\ell_n(k_y)$, where $\ell_n(k_y) \equiv \sqrt{3}(J-1)k_y a/2 - n\pi$ for $J = 20$. We can see that along $k_y \in (0, 2\pi/\sqrt{3}a)$, ϕ_0 for $k_x = 0.83\pi/a$ [0.91 π/a] does not intersect $-\ell_J$ [$-\ell_J$ and $-\ell_{J-1}$], thus two [four] bulk states are missing in the dispersive bands.

To demonstrate that the edge states arise from the missing missing bulk states, we substitute $k_y = 2\pi/\sqrt{3}a + i\kappa_y$ into Eq. (A12). The existence of edge states requires

$$\begin{aligned} \delta_0(\kappa_y) &\equiv \beta^2 - \frac{\sinh(\sqrt{3}J\kappa_y a/2)}{\sinh(\rho\kappa_y)}\beta + \frac{\sinh(\mathcal{L}_y\kappa_y)}{\sinh(\rho\kappa_y)}\frac{\sin^2(2\vartheta)}{4} \\ &= 0. \end{aligned} \quad (\text{A17})$$

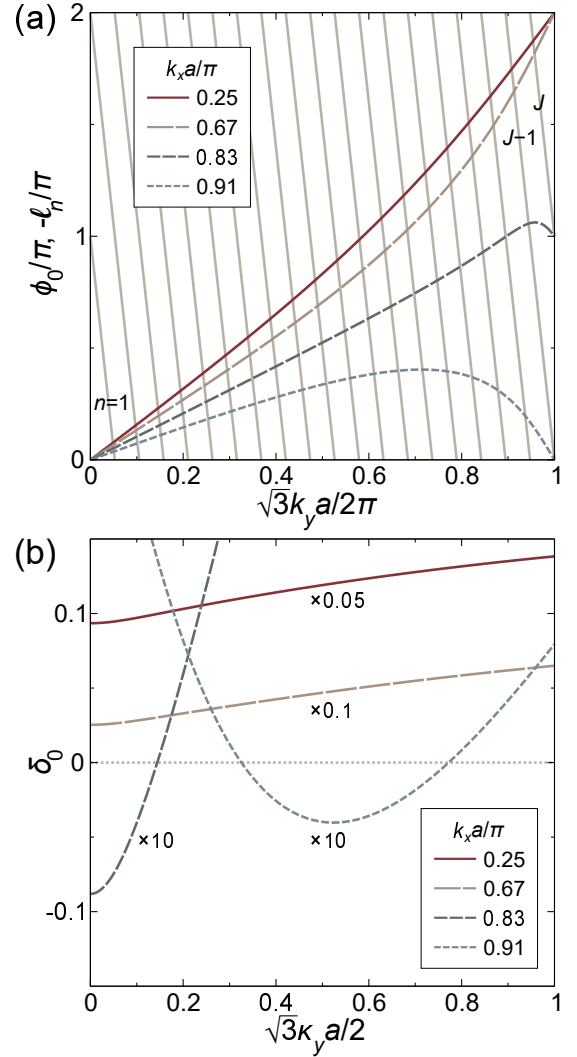


FIG. 15. (a) Plot of $\phi_0(\mathbf{k})$ as a function of k_y for $k_x = 0.25\pi/a, 0.67\pi/a, 0.83\pi/a$ and $0.91\pi/a$, where $\alpha = 0.8$. The straight lines are $-\ell_n(k_y) = -\sqrt{3}(J-1)k_y a/2 + n\pi$, $n = 1, \dots, J$, for $J = 20$. (b) Plot of $\delta_0(\kappa_y)$ for the same k_x 's.

Fig. 15(b) shows $\delta_0(\kappa_y)$ for several k_x 's. The number of zero-crossings for $k_x = 0.83\pi/a$ [0.91 π/a] is one [two], which indicates the existence of two [four] edge states.

For $J\kappa_y a \gg 1$, Eq. (A17) is rearranged into

$$e^{2\kappa_y} \beta^2 - e^{\kappa_y} \beta + \sin^2(2\vartheta)/4 = 0. \quad (\text{A18})$$

It is noted that Eqs. (A18) and (A15) become identical in the limits $\kappa_y \rightarrow 0$ and $J \rightarrow \infty$, respectively. The solutions of Eq. (A18) are given by

$$\kappa_y^+ = \ln(\cos^2\vartheta/\beta), \quad (\text{A19a})$$

$$\kappa_y^- = \ln(\sin^2\vartheta/\beta). \quad (\text{A19b})$$

By substituting κ_y^\pm into Eq. (64), the energies of edge

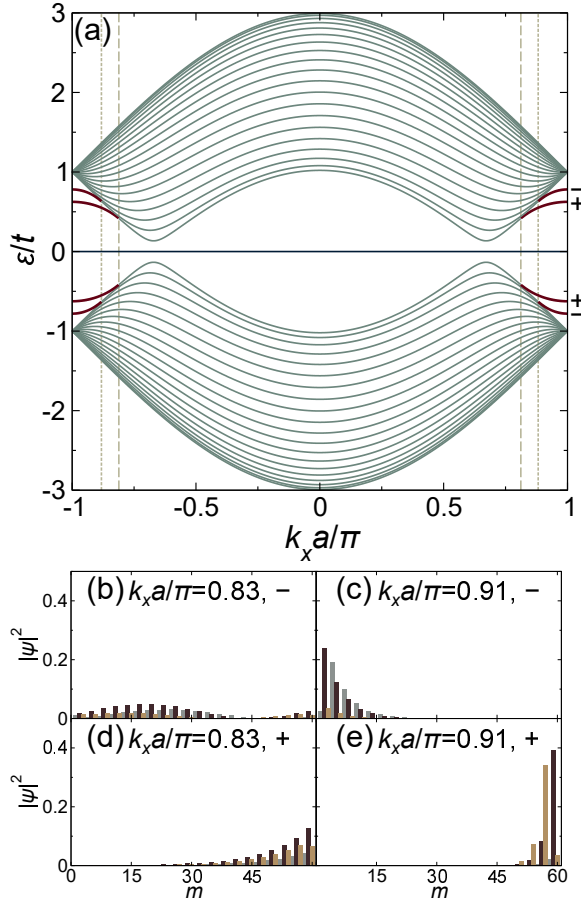


FIG. 16. (a) Energy spectra of the ABC ZR as a function of k_x for $\alpha = 0.8$ and $J = 20$. The bold red lines indicate the edge states. The blue line at $\varepsilon = 0$ is the flat band. The transitions from bulk to edge states for the "+" ["-"] bands occur at $|k_x| \approx 0.8116\pi/a$ [$0.8818\pi/a$], marked by the vertical dashed [dotted] lines. (b) and (c) [(d) and (e)] Probability density $|\psi|^2$ per site m for the "-" ["+"] bands at $k_x = 0.83\pi/a$ and $0.91\pi/a$, respectively.

states are given as follows:

$$\tilde{\varepsilon}_s^+ = st_C \sqrt{1 - (\beta/\cos\vartheta)^2}, \quad (\text{A20a})$$

$$\tilde{\varepsilon}_s^- = st_A \sqrt{1 - (\beta/\sin\vartheta)^2}. \quad (\text{A20b})$$

Since $\kappa_y^\pm > 0$, the edge states associated with $\tilde{\varepsilon}_s^\pm$ appear in the range $\chi_{20}^\pm < |k_x| \leq \pi/a$, where $t_C \sin\vartheta < |\tilde{\varepsilon}_s^+| \leq t_C$ and $t_A \cos\vartheta < |\tilde{\varepsilon}_s^-| \leq t_A$. Note that for $\alpha = 0$, the edge states with $\tilde{\varepsilon}_s^-$ vanish. The remaining edge states with $\tilde{\varepsilon}_s^+ = 0$ exist for $|k_x| \in (2\pi/3a, \pi/a]$ because the ABC ZR reduces to the graphene ZR by removing the C sites.

Fig. 16(a) shows the numerical calculation of energy spectra as a function of k_x . The vertical dashed and dotted lines accordingly mark $\chi_{20}^+ \approx 0.8116\pi/a$ and $\chi_{20}^- \approx 0.8818\pi/a$. The bold red lines in the bands labeled by "+" and "-" depict the edge states with energies $\tilde{\varepsilon}_s^+$ and $\tilde{\varepsilon}_s^-$, respectively. At $|k_x| = \pi/a$, the edge states are pinned at $\varepsilon = t_C \approx 0.6247t$ and $\varepsilon = t_A \approx 0.7809t$, con-

sistent with Eqs. (A20a) and (A20b).

Figs. 16(b) and (c) [(d) and (e)] depict the probability density $|\psi|^2$ per site m for the "-" ["+"] bands at $k_x = 0.83\pi/a$ and $0.91\pi/a$, respectively. Since $0.83\pi/a < \chi_{20}^- < 0.91\pi/a$, Figs. 16(b) and (c) accordingly show the profile of bulk and edge states. On the other hand, both Figs. 16(d) and (e) exhibit the profile of edge states because $\chi_{20}^+ < 0.83\pi/a < 0.91\pi/a$.

APPENDIX B: DERIVATIONS OF EQS. (53), (66)

First, let us determine \mathcal{A}' and \mathbf{k}' in $\psi_s(\mathbf{r})$ [see Eq. (43)]. Eqs. (48) or (51) imply $\mathcal{A}' = -\mathcal{A}$ and $\mathbf{k} \cdot \mathbf{a}_1 = \mathbf{k}' \cdot \mathbf{a}_1$, due to the conservation of momentum in the x direction. It can be shown that the conservation of energy $\varepsilon(\mathbf{k}) = \varepsilon(\mathbf{k}')$ gives $\mathbf{k} \cdot \mathbf{a}_1 = \mathbf{k}' \cdot \mathbf{a}_1 = (\mathbf{k} + \mathbf{k}') \cdot \mathbf{a}_2$ [see Eq. (37a)]. By using the vector components of \mathbf{a}_1 and \mathbf{a}_2 , we get

$$\mathbf{k} = (k_x, k_y), \text{ and } \mathbf{k}' = (k_x, -k_y). \quad (\text{B1})$$

Next, we write Eq. (35) as $f(\mathbf{k}) = e^{-i\mathbf{k} \cdot \mathbf{b}_n} g_n(\mathbf{k})$, where

$$g_1(\mathbf{k}) = 1 + e^{-i\mathbf{k} \cdot \mathbf{a}_1} + e^{-i\mathbf{k} \cdot \mathbf{a}_2} = q(\mathbf{k})e^{-i\mathbf{k} \cdot \mathbf{a}_1/2}, \quad (\text{B2})$$

$$g_2(\mathbf{k}) = 1 + e^{i\mathbf{k} \cdot \mathbf{a}_1} + e^{i\mathbf{k} \cdot (\mathbf{a}_1 - \mathbf{a}_2)} = q(\mathbf{k})e^{i\mathbf{k} \cdot \mathbf{a}_1/2}, \quad (\text{B3})$$

$$g_3(\mathbf{k}) = 1 + e^{i\mathbf{k} \cdot \mathbf{a}_2} + e^{i\mathbf{k} \cdot (\mathbf{a}_2 - \mathbf{a}_1)} = p^*(\mathbf{k}). \quad (\text{B4})$$

Note that $|g_n(\mathbf{k})| = |f(\mathbf{k})|$. $p(\mathbf{k})$ and $q(\mathbf{k})$ are defined in Eqs. (75) and (76), respectively.

1. Derivation of Eq. (53)

Let us express $\psi_s(\mathbf{r})$ in terms of $|\psi_s(\mathbf{k})\rangle$ [see Eq. (38a)]. Multiplying Eq. (47) by $|f(\mathbf{k})|$ yields

$$e^{-i\mathbf{k} \cdot \mathbf{L}} f(\mathbf{k}) - e^{-i\mathbf{k}' \cdot \mathbf{L}} f(\mathbf{k}') + e^{-i\mathbf{k} \cdot (\mathbf{L} + \mathbf{a}_1)} f(\mathbf{k}) - e^{-i\mathbf{k}' \cdot (\mathbf{L} + \mathbf{a}_1)} f(\mathbf{k}') + \alpha^2 \{e^{-i\mathbf{k} \cdot (\mathbf{L} - \mathbf{b}_1)} f^*(\mathbf{k}) - e^{-i\mathbf{k}' \cdot (\mathbf{L} - \mathbf{b}_1)} f^*(\mathbf{k}')\} = 0. \quad (\text{B5})$$

In the middle unit cell in Fig. 5(a), the A and C sites are connected to the B site by \mathbf{b}_3 and \mathbf{b}_1 , respectively. By expressing f (f^*) in terms of g_3 (g_1^*), Eq. (B5) becomes

$$\{1 + e^{-ik_x a}\} \{e^{-ik_y \rho} g_3(\mathbf{k}) - e^{ik_y \rho} g_3(\mathbf{k}')\} + \alpha^2 e^{-ik_x a} \{e^{-ik_y \rho} g_1^*(\mathbf{k}) - e^{ik_y \rho} g_1^*(\mathbf{k}')\} = 0. \quad (\text{B6})$$

Multiplying Eq. (B6) by $e^{ik_x a/2}$ and grouping the resulting terms gives Eq. (53).

2. Derivation of Eq. (66)

By following the same procedure, we multiply Eq. (52) by $|f(\mathbf{k})|$ as follows:

$$e^{i\mathbf{k} \cdot (\mathbf{L} - \mathbf{b}_2)} f(\mathbf{k}) - e^{i\mathbf{k}' \cdot (\mathbf{L} - \mathbf{b}_2)} f(\mathbf{k}') + \alpha^2 \{e^{i\mathbf{k} \cdot \mathbf{L}} f^*(\mathbf{k}) - e^{i\mathbf{k}' \cdot \mathbf{L}} f^*(\mathbf{k}')\} + \alpha^2 \{e^{i\mathbf{k} \cdot (\mathbf{L} - \mathbf{a}_1)} f^*(\mathbf{k}) - e^{i\mathbf{k}' \cdot (\mathbf{L} - \mathbf{a}_1)} f^*(\mathbf{k}')\} = 0. \quad (\text{B7})$$

In the top unit cell in Fig. 5(a), the A (C) site is connected the B site by \mathbf{b}_2 (\mathbf{b}_3). Hence, f and f^* in Eq. (B7)

are expressed in terms of g_2 and g_3^* , respectively,

$$e^{-ik_x a} \{e^{ik_y \rho} g_2(\mathbf{k}) - e^{-ik_y \rho} g_2(\mathbf{k}')\} + \alpha^2 \{1 + e^{-ik_x a}\} \{e^{ik_y \rho} g_3^*(\mathbf{k}) - e^{-ik_y \rho} g_3^*(\mathbf{k}')\} = 0. \quad (\text{B8})$$

Multiplying Eq. (B8) by $e^{ik_x a/2}$ and grouping the resulting terms leads to Eq. (66).

-
- [1] M. Z. Hasan and C. L. Kane, “Colloquium: topological insulators,” *Rev. Mod. Phys.* **82**, 3045 (2010).
- [2] N. Cooper, J. Dalibard, and I. Spielman, “Topological bands for ultracold atoms,” *Rev. Mod. Phys.* **91**, 015005 (2019).
- [3] J. Cayssol and J.-N. Fuchs, “Topological and geometrical aspects of band theory,” *J. Phys. Mater.* **4**, 034007 (2021).
- [4] D. J. Thouless, M. Kohmoto, M. P. Nightingale, and M. den Nijs, “Quantized Hall conductance in a two-dimensional periodic potential,” *Phys. Rev. Lett.* **49**, 405 (1982).
- [5] K. v. Klitzing, G. Dorda, and M. Pepper, “New method for high-accuracy determination of the fine-structure constant based on quantized Hall resistance,” *Phys. Rev. Lett.* **45**, 494 (1980).
- [6] C. L. Kane and E. J. Mele, “Quantum spin Hall effect in graphene,” *Phys. Rev. Lett.* **95**, 226801 (2005).
- [7] M. V. Berry, “Quantal phase factors accompanying adiabatic changes,” *Proc. R. Soc. A: Math. Phys. Eng. Sci.* **392**, 45 (1984).
- [8] J. Zak, “Berry’s phase for energy bands in solids,” *Phys. Rev. Lett.* **62**, 2747 (1989).
- [9] D. Xiao, M.-C. Chang, and Q. Niu, “Berry phase effects on electronic properties,” *Rev. Mod. Phys.* **82**, 1959 (2010).
- [10] W.-P. Su, J. R. Schrieffer, and A. J. Heeger, “Solitons in polyacetylene,” *Phys. Rev. Lett.* **42**, 1698 (1979).
- [11] P. Delplace, D. Ullmo, and G. Montambaux, “Zak phase and the existence of edge states in graphene,” *Phys. Rev. B* **84**, 195452 (2011).
- [12] T. Cao, F. Zhao, and S. G. Louie, “Topological phases in graphene nanoribbons: junction states, spin centers, and quantum spin chains,” *Phys. Rev. Lett.* **119**, 076401 (2017).
- [13] O. Gröning, S. Wang, X. Yao, C. A. Pignedoli, G. Borin Barin, C. Daniels, A. Cupo, V. Meunier, X. Feng, A. Narita, *et al.*, “Engineering of robust topological quantum phases in graphene nanoribbons,” *Nature* **560**, 209 (2018).
- [14] J. Li, S. Sanz, N. Merino-Díez, M. Vilas-Varela, A. Garcia-Lekue, M. Corso, D. G. de Oteyza, T. Frederiksen, D. Peña, and J. I. Pascual, “Topological phase transition in chiral graphene nanoribbons: from edge bands to end states,” *Nat. Commun.* **12**, 5538 (2021).
- [15] J.-W. Rhim, J. H. Bardarson, and R.-J. Slager, “Unified bulk-boundary correspondence for band insulators,” *Phys. Rev. B* **97**, 115143 (2018).
- [16] S. Ryu and Y. Hatsugai, “Topological origin of zero-energy edge states in particle-hole symmetric systems,” *Phys. Rev. Lett.* **89**, 077002 (2002).
- [17] R. S. Mong and V. Shivamoggi, “Edge states and the bulk-boundary correspondence in Dirac Hamiltonians,” *Phys. Rev. B* **83**, 125109 (2011).
- [18] M. Ezawa, “Topological origin of quasi-flat edge band in phosphorene,” *New J. Phys.* **16**, 115004 (2014).
- [19] M. M. Grujić, M. Ezawa, M. Ž. Tadić, and F. M. Peeters, “Tunable skewed edges in puckered structures,” *Phys. Rev. B* **93**, 245413 (2016).
- [20] G. van Miert, C. Ortix, and C. M. Smith, “Topological origin of edge states in two-dimensional inversion-symmetric insulators and semimetals,” *2D Mater.* **4**, 015023 (2016).
- [21] M. Hitomi, T. Kawakami, and M. Koshino, “Multi-orbital edge and corner states in black phosphorene,” *Phys. Rev. B* **104**, 125302 (2021).
- [22] M. Atala, M. Aidelsburger, J. T. Barreiro, D. Abanin, T. Kitagawa, E. Demler, and I. Bloch, “Direct measurement of the Zak phase in topological Bloch bands,” *Nat. Phys.* **9**, 795 (2013).
- [23] F. Grusdt, D. Abanin, and E. Demler, “Measuring \mathbb{Z}_2 topological invariants in optical lattices using interferometry,” *Phys. Rev. A* **89**, 043621 (2014).
- [24] H.-I. Lu, M. Schemmer, L. M. Ayccock, D. Genkina, S. Sugawa, and I. B. Spielman, “Geometrical pumping with a bose-einstein condensate,” *Phys. Rev. Lett.* **116**, 200402 (2016).
- [25] E. J. Meier, F. A. An, and B. Gadway, “Observation of the topological soliton state in the Su-Schrieffer-Heeger model,” *Nat. Commun.* **7**, 13986 (2016).
- [26] F. Mivehvar, H. Ritsch, and F. Piazza, “Superradiant topological peierls insulator inside an optical cavity,” *Phys. Rev. Lett.* **118**, 073602 (2017).
- [27] P. St-Jean, V. Goblot, E. Galopin, A. Lemaître, T. Ozawa, L. Le Gratiet, I. Sagnes, J. Bloch, and A. Amo, “Lasing in topological edge states of a one-dimensional lattice,” *Nat. Photonics* **11**, 651 (2017).
- [28] S. Longhi, “Probing one-dimensional topological phases in waveguide lattices with broken chiral symmetry,” *Opt. Lett.* **43**, 4639 (2018).
- [29] J. Jiang, Z. Guo, Y. Ding, Y. Sun, Y. Li, H. Jiang, and H. Chen, “Experimental demonstration of the robust edge states in a split-ring-resonator chain,” *Opt. Express* **26**, 12891 (2018).
- [30] Z.-Q. Jiao, S. Longhi, X.-W. Wang, J. Gao, W.-H. Zhou, Y. Wang, Y.-X. Fu, L. Wang, R.-J. Ren, L.-F. Qiao, *et al.*, “Experimentally detecting quantized Zak phases without chiral symmetry in photonic lattices,” *Phys. Rev. Lett.* **127**, 147401 (2021).
- [31] T. Goren, K. Plekhanov, F. Appas, and K. Le Hur, “Topological Zak phase in strongly coupled LC circuits,” *Phys. Rev. B* **97**, 041106 (2018).

- [32] C. Tao, L. Jiao, O. V. Yazyev, Y.-C. Chen, J. Feng, X. Zhang, R. B. Capaz, J. M. Tour, A. Zettl, S. G. Louie, *et al.*, “Spatially resolving edge states of chiral graphene nanoribbons,” *Nat. Phys.* **7**, 616 (2011).
- [33] S. Wang, L. Talirz, C. A. Pignedoli, X. Feng, K. Müllen, R. Fasel, and P. Ruffieux, “Giant edge state splitting at atomically precise graphene zigzag edges,” *Nat. Commun.* **7**, 11507 (2016).
- [34] V. S. Prudkovskiy, Y. Hu, K. Zhang, Y. Hu, P. Ji, G. Nunn, J. Zhao, C. Shi, A. Tejada, D. Wander, *et al.*, “An epitaxial graphene platform for zero-energy edge state nanoelectronics,” *Nat. Commun.* **13**, 7814 (2022).
- [35] M. Polini, F. Guinea, M. Lewenstein, H. C. Manoharan, and V. Pellegrini, “Artificial honeycomb lattices for electrons, atoms and photons,” *Nat. Nanotechnol.* **8**, 625 (2013).
- [36] M. C. Rechtsman, Y. Plotnik, J. M. Zeuner, D. Song, Z. Chen, A. Szameit, and M. Segev, “Topological creation and destruction of edge states in photonic graphene,” *Phys. Rev. Lett.* **111**, 103901 (2013).
- [37] Y. Plotnik, M. C. Rechtsman, D. Song, M. Heinrich, J. M. Zeuner, S. Nolte, Y. Lumer, N. Malkova, J. Xu, A. Szameit, *et al.*, “Observation of unconventional edge states in ‘photonic graphene,’” *Nat. Mater.* **13**, 57 (2014).
- [38] M. Bellec, U. Kuhl, G. Montambaux, and F. Mortessagne, “Manipulation of edge states in microwave artificial graphene,” *New J. Phys.* **16**, 113023 (2014).
- [39] M. Milićević, T. Ozawa, G. Montambaux, I. Carusotto, E. Galopin, A. Lemaitre, L. Le Gratiet, I. Sagnes, J. Bloch, and A. Amo, “Orbital edge states in a photonic honeycomb lattice,” *Phys. Rev. Lett.* **118**, 107403 (2017).
- [40] Z. Zhang, R. Wang, Y. Zhang, Y. V. Kartashov, F. Li, H. Zhong, H. Guan, K. Gao, F. Li, Y. Zhang, *et al.*, “Observation of edge solitons in photonic graphene,” *Nat. Commun.* **11**, 1902 (2020).
- [41] S. Xia, Y. Liang, L. Tang, D. Song, J. Xu, and Z. Chen, “Photonic realization of a generic type of graphene edge states exhibiting topological flat band,” *Phys. Rev. Lett.* **131**, 013804 (2023).
- [42] X. Xi, J. Ma, S. Wan, C.-H. Dong, and X. Sun, “Observation of chiral edge states in gapped nanomechanical graphene,” *Sci. Adv.* **7**, eabe1398 (2021).
- [43] G. Wang, Z. Zhang, Y. Gu, D. Liao, Y. Cheng, and X. Liu, “Zak-phase-inspired acoustic topological edge states on the honeycomb lattice,” *Phys. Rev. B* **103**, 094102 (2021).
- [44] D. Han, Y. Lai, J. Zi, Z.-Q. Zhang, and C. T. Chan, “Dirac spectra and edge states in honeycomb plasmonic lattices,” *Phys. Rev. Lett.* **102**, 123904 (2009).
- [45] L. Wang, R.-Y. Zhang, M. Xiao, D. Han, C. T. Chan, and W. Wen, “The existence of topological edge states in honeycomb plasmonic lattices,” *New J. Phys.* **18**, 103029 (2016).
- [46] T. Jacqmin, I. Carusotto, I. Sagnes, M. Abbarchi, D. Solnyshkov, G. Malpuech, E. Galopin, A. Lemaitre, J. Bloch, and A. Amo, “Direct observation of Dirac cones and a flatband in a honeycomb lattice for polaritons,” *Phys. Rev. Lett.* **112**, 116402 (2014).
- [47] P. St-Jean, A. Dauphin, P. Massignan, B. Real, O. Jamadi, M. Milicevic, A. Lemaitre, A. Harouri, L. Le Gratiet, I. Sagnes, *et al.*, “Measuring topological invariants in a polaritonic analog of graphene,” *Phys. Rev. Lett.* **126**, 127403 (2021).
- [48] A. Raoux, M. Morigi, J.-N. Fuchs, F. Piéchon, and G. Montambaux, “From dia-to paramagnetic orbital susceptibility of massless fermions,” *Phys. Rev. Lett.* **112**, 026402 (2014).
- [49] A. C. Neto, F. Guinea, N. M. Peres, K. S. Novoselov, and A. K. Geim, “The electronic properties of graphene,” *Rev. Mod. Phys.* **81**, 109 (2009).
- [50] D. Bercioux, D. Urban, H. Grabert, and W. Häusler, “Massless Dirac-Weyl fermions in α - T_3 optical lattice,” *Phys. Rev. A* **80**, 063603 (2009).
- [51] B. Dóra, J. Kailasvuori, and R. Moessner, “Lattice generalization of the Dirac equation to general spin and the role of the flat band,” *Phys. Rev. B* **84**, 195422 (2011).
- [52] D. F. Urban, D. Bercioux, M. Wimmer, and W. Häusler, “Barrier transmission of Dirac-like pseudospin-one particles,” *Phys. Rev. B* **84**, 115136 (2011).
- [53] A. Fang, Z. Zhang, S. G. Louie, and C. T. Chan, “Klein tunneling and supercollimation of pseudospin-1 electromagnetic waves,” *Phys. Rev. B* **93**, 035422 (2016).
- [54] E. Illes and E. Nicol, “Klein tunneling in the α - T_3 model,” *Phys. Rev. B* **95**, 235432 (2017).
- [55] Y. Betancur-Ocampo, G. Cordourier-Maruri, V. Gupta, and R. de Coss, “Super-Klein tunneling of massive pseudospin-one particles,” *Phys. Rev. B* **96**, 024304 (2017).
- [56] N. Weekes, A. Iurov, L. Zhemchuzhna, G. Gumbs, and D. Huang, “Generalized wkb theory for electron tunneling in gapped α - T_3 lattices,” *Phys. Rev. B* **103**, 165429 (2021).
- [57] S. Cunha, D. da Costa, J. M. Pereira Jr, R. Costa Filho, B. Van Duppen, and F. Peeters, “Tunneling properties in α - T_3 lattices: Effects of symmetry-breaking terms,” *Phys. Rev. B* **105**, 165402 (2022).
- [58] E. Illes, J. Carbotte, and E. Nicol, “Hall quantization and optical conductivity evolution with variable Berry phase in the α - T_3 model,” *Phys. Rev. B* **92**, 245410 (2015).
- [59] J. Malcolm and E. Nicol, “Frequency-dependent polarizability, plasmons, and screening in the two-dimensional pseudospin-1 dice lattice,” *Phys. Rev. B* **93**, 165433 (2016).
- [60] J. Carbotte, K. Bryenton, and E. Nicol, “Optical properties of a semi-Dirac material,” *Phys. Rev. B* **99**, 115406 (2019).
- [61] M. Mojarro, V. Ibarra-Sierra, J. Sandoval-Santana, R. Carrillo-Bastos, and G. G. Naumis, “Electron transitions for Dirac Hamiltonians with flat bands under electromagnetic radiation: Application to the α - T_3 graphene model,” *Phys. Rev. B* **101**, 165305 (2020).
- [62] C.-D. Han and Y.-C. Lai, “Optical response of two-dimensional Dirac materials with a flat band,” *Phys. Rev. B* **105**, 155405 (2022).
- [63] A. Iurov, L. Zhemchuzhna, G. Gumbs, D. Huang, D. Dahal, and Y. Abranyos, “Finite-temperature plasmons, damping, and collective behavior in the α - T_3 model,” *Phys. Rev. B* **105**, 245414 (2022).
- [64] D. Oriekhov and V. Gusynin, “Optical conductivity of semi-Dirac and pseudospin-1 models: Zitterbewegung approach,” *Phys. Rev. B* **106**, 115143 (2022).
- [65] A. Iurov, L. Zhemchuzhna, G. Gumbs, D. Huang, P. Fekete, F. Anwar, D. Dahal, and N. Weekes, “Tailoring plasmon excitations in α - T_3 armchair nanoribbons,”

- Sci. Rep. **11**, 20577 (2021).
- [66] E. Illes and E. Nicol, “Magnetic properties of the α - T_3 model: Magneto-optical conductivity and the hofstadter butterfly,” Phys. Rev. B **94**, 125435 (2016).
- [67] R. Soni, N. Kaushal, S. Okamoto, and E. Dagotto, “Flat bands and ferrimagnetic order in electronically correlated dice-lattice ribbons,” Phys. Rev. B **102**, 045105 (2020).
- [68] O. Roslyak, G. Gumbs, A. Balassis, and H. Elsayed, “Effect of magnetic field and chemical potential on the rkky interaction in the α - T_3 lattice,” Phys. Rev. B **103**, 075418 (2021).
- [69] J. Sun, T. Liu, Y. Du, and H. Guo, “Strain-induced pseudo magnetic field in the α - T_3 lattice,” Phys. Rev. B **106**, 155417 (2022).
- [70] A. Filusch and H. Fehske, “Tunable valley filtering in dynamically strained α - T_3 lattices,” Phys. Rev. B **106**, 245106 (2022).
- [71] R. Li, J.-F. Liu, and J. Wang, “Topological ac charge current and continuous invariant in the α - T_3 lattice under a periodically varying strain,” Phys. Rev. B **108**, 115403 (2023).
- [72] Á. D. Kovács, G. Dávid, B. Dóra, and J. Cserti, “Frequency-dependent magneto-optical conductivity in the generalized α - T_3 model,” Phys. Rev. B **95**, 035414 (2017).
- [73] Y.-R. Chen, Y. Xu, J. Wang, J.-F. Liu, and Z. Ma, “Enhanced magneto-optical response due to the flat band in nanoribbons made from the α - T_3 lattice,” Phys. Rev. B **99**, 045420 (2019).
- [74] L. Chen, J. Zuber, Z. Ma, and C. Zhang, “Nonlinear optical response of the α - T_3 model due to the nontrivial topology of the band dispersion,” Phys. Rev. B **100**, 035440 (2019).
- [75] A. Balassis, D. Dahal, G. Gumbs, A. Iurov, D. Huang, and O. Roslyak, “Magnetoplasmons for the α - T_3 model with filled landau levels,” J. Phys.: Condens. Matter **32**, 485301 (2020).
- [76] M. Vigh, L. Oroszlány, S. Vajna, P. San-Jose, G. Dávid, J. Cserti, and B. Dóra, “Diverging dc conductivity due to a flat band in a disordered system of pseudospin-1 Dirac-Weyl fermions,” Phys. Rev. B **88**, 161413 (2013).
- [77] T. Louvet, P. Delpierre, A. A. Fedorenko, and D. Carpentier, “On the origin of minimal conductivity at a band crossing,” Phys. Rev. B **92**, 155116 (2015).
- [78] J. J. Wang, S. Liu, J. Wang, and J.-F. Liu, “Integer quantum Hall effect of the α - T_3 model with a broken flat band,” Phys. Rev. B **102**, 235414 (2020).
- [79] X.-H. Wang, J. J. Wang, J. Wang, and J.-F. Liu, “Flat band assisted topological charge pump in the dice lattice,” Phys. Rev. B **103**, 195442 (2021).
- [80] X. Zhou, “Andreev reflection and Josephson effect in the α - T_3 lattice,” Phys. Rev. B **104**, 125441 (2021).
- [81] T. Biswas and T. K. Ghosh, “Magnetotransport properties of the α - T_3 model,” J. Phys.: Condens. Matter **28**, 495302 (2016).
- [82] S. F. Islam and P. Dutta, “Valley-polarized magnetoconductivity and particle-hole symmetry breaking in a periodically modulated α - T_3 lattice,” Phys. Rev. B **96**, 045418 (2017).
- [83] W. Duan, “Seebeck and Nernst effects of pseudospin-1 fermions in the α - T_3 model under magnetic fields,” Phys. Rev. B **108**, 155428 (2023).
- [84] D. Huang, A. Iurov, H.-Y. Xu, Y.-C. Lai, and G. Gumbs, “Interplay of Lorentz-Berry forces in position-momentum spaces for valley-dependent impurity scattering in α - T_3 lattices,” Phys. Rev. B **99**, 245412 (2019).
- [85] F. Wang and Y. Ran, “Nearly flat band with chern number $C = 2$ on the dice lattice,” Phys. Rev. B **84**, 241103 (2011).
- [86] O. Köksal, L. Li, and R. Pentcheva, “High chern numbers in a perovskite-derived dice lattice $(\text{LaXO}_3)_3/(\text{LaAlO}_3)_3(111)$ with X= Ti, Mn and Co,” Sci. Rep. **13**, 10615 (2023).
- [87] L. Zhu, S.-S. Wang, S. Guan, Y. Liu, T. Zhang, G. Chen, and S. A. Yang, “Blue phosphorene oxide: strain-tunable quantum phase transitions and novel 2d emergent fermions,” Nano Lett. **16**, 6548 (2016).
- [88] J. D. Malcolm and E. J. Nicol, “Magneto-optics of massless Kane fermions: Role of the flat band and unusual Berry phase,” Phys. Rev. B **92**, 035118 (2015).
- [89] M. Orlita, D. Basko, M. Zholudev, F. Teppe, W. Knap, V. Gavrilenko, N. Mikhailov, S. Dvoretzki, P. Neugebauer, C. Faugeras, *et al.*, “Observation of three-dimensional massless kane fermions in a zinc-blende crystal,” Nat. Phys. **10**, 233 (2014).
- [90] T. Andrijauskas, E. Anisimovas, M. Račiūnas, A. Mekys, V. Kudriašov, I. Spielman, and G. Juzeliūnas, “Three-level Haldane-like model on a dice optical lattice,” Phys. Rev. A **92**, 033617 (2015).
- [91] B. Dey, P. Kapri, O. Pal, and T. K. Ghosh, “Unconventional phases in a Haldane model of dice lattice,” Phys. Rev. B **101**, 235406 (2020).
- [92] F. D. M. Haldane, “Model for a quantum Hall effect without Landau levels: Condensed-matter realization of the” parity anomaly”, Phys. Rev. Lett. **61**, 2015 (1988).
- [93] J. Wang and J.-F. Liu, “Quantum spin Hall phase transition in the α - T_3 lattice,” Phys. Rev. B **103**, 075419 (2021).
- [94] L. Hao, “Zigzag dice lattice ribbons: Distinct edge morphologies and structure-spectrum correspondences,” Phys. Rev. Mater. **6**, 034002 (2022).
- [95] B. Real, C. Cantillano, D. López-González, A. Szameit, M. Aono, M. Naruse, S.-J. Kim, K. Wang, and R. A. Vicencio, “Flat-band light dynamics in stub photonic lattices,” Sci. Rep. **7**, 15085 (2017).
- [96] J. Bartlett, H. Hu, and E. Zhao, “Illuminating the bulk-boundary correspondence of a non-hermitian stub lattice with Majorana stars,” Phys. Rev. B **104**, 195131 (2021).
- [97] G. Cáceres-Aravena, B. Real, D. Guzmán-Silva, A. Amo, L. E. F. Torres, and R. A. Vicencio, “Experimental observation of edge states in SSH-stub photonic lattices,” Phys. Rev. Res. **4**, 013185 (2022).
- [98] E. Majorana, “Atomi orientati in campo magnetico variabile,” Il Nuovo Cimento (1924-1942) **9**, 43 (1932).
- [99] J. Hannay, “The Berry phase for spin in the Majorana representation,” J. Phys. A: Math. Gen. **31**, L53 (1998).
- [100] H. Liu and L. Fu, “Representation of Berry phase by the trajectories of Majorana stars,” Phys. Rev. Lett. **113**, 240403 (2014).
- [101] F. R. Pratama and T. Nakanishi, “Topological edge state of massless fermion with non-quantized and zero Berry phases,” Submitted (2024).

- [102] The positions of all sites in each unit cell are regarded as identical. This treatment is equivalent to fixing a gauge in the Hamiltonian such that the intracell hopping is real [11, 18].
- [103] $Z = \text{Arg}(X + iY) = \text{atan2}(Y, X)$, where atan2 is two-argument arctangent function. Particularly, $Z = 0$ for $Y = 0, X > 0$ and $Z = \pi$ for $Y = 0, X < 0$.
- [104] For $V'_A < 0$, the BZ is defined for $k \in [0, 2\pi/a_0]$, because $F(k) = V_A - |V'_A|e^{-ik a_0} = V_A + |V'_A|e^{-i(k+\pi/a_0)a_0}$.
- [105] E. H. Lieb, “Two theorems on the hubbard model,” *Phys. Rev. Lett.* **62**, 1201 (1989).
- [106] K. Wakabayashi, K.-i. Sasaki, T. Nakanishi, and T. Enoki, “Electronic states of graphene nanoribbons and analytical solutions,” *Sci. Technol. Adv. Mater.* **11**, 054504 (2010).
- [107] J. Schwinger, “On angular momentum,” US Atomic Energy Commission, Report No. NYO-3071 (1952).
- [108] M. Ezawa, Y. Tanaka, and N. Nagaosa, “Topological phase transition without gap closing,” *Sci. Rep.* **3**, 2790 (2013).
- [109] S. Longhi, “Aharonov-Bohm photonic cages in waveguide and coupled resonator lattices by synthetic magnetic fields,” *Opt. Lett.* **39**, 5892 (2014).
- [110] S. Mukherjee and R. R. Thomson, “Observation of localized flat-band modes in a quasi-one-dimensional photonic rhombic lattice,” *Opt. Lett.* **40**, 5443 (2015).
- [111] G. Pelegrí, A. Marques, R. Dias, A. Daley, V. Ahufinger, and J. Mompart, “Topological edge states with ultracold atoms carrying orbital angular momentum in a diamond chain,” *Phys. Rev. A* **99**, 023612 (2019).
- [112] D. Orikhov, E. Gorbar, and V. Gusynin, “Electronic states of pseudospin-1 fermions in dice lattice ribbon,” *Low Temp. Phys.* **44**, 1313 (2018).